Proteus Magnets for Fluid Composition and Fluid Flow Measurements

by

Michael Ross

B.Sc., Mount Allison University, 2018

A Thesis Submitted in Partial Fulfilment of the Requirements for the Degree of

Master of Science

In the Graduate Academic Unit of Physics

Supervisor:	Bruce Balcom, Ph.D., Physics
Examining Board:	William Ward, Ph.D., Physics
	David Burns, Ph.D., Chemistry

This thesis is accepted by the Dean of Graduate Studies

THE UNIVERSITY OF NEW BRUNSWICK

April 2021

Abstract

In this thesis, the design, fabrication, and testing of a new portable magnet, generically termed the Proteus magnet, is presented as means of performing a broad range of magnetic resonance measurements. The Proteus magnet is intended for ^{1}H measurements of liquids and is fully functional when submersed in the sample of interest. The Proteus magnet is fabricated from a pair of low-cost, commercial, NdFeB disk magnets, axially polarized, with their North and South poles aligned. The sensor is evaluated through a series of measurements including bulk Carr-Purcell-Meiboom-Gill (CPMG), T_2, saturation recovery T_1, self-diffusion, $T_1 - T_2$, and $D - T_2$. The Proteus magnet geometry was altered to introduce a moderate 65 gauss/cm constant gradient to permit the acquisition of phase shifted magnetic resonance signal from fluids flowing through the magnet with CPMG measurements. The mean flow velocity can be determined from the phase shift.

Acknowledgements

I would like to thank my supervisor, Dr. Bruce Balcom, for his guidance throughout the course of my studies. I would like to acknowledge my colleagues, Dr. Jiangfeng Guo and Andrés Aguilera whose discussions and suggestions helped further my understanding. I would like to express my gratitude to my parents for their love and support. Lastly, I would like to thank my girlfriend who helped me every step of the way.

I would like to personally thank the New Brunswick Innovation Fund for a research assistantship [RAI 2019-044]. Funding from the Natural Sciences and Engineering Research Council of Canada, through a Discovery grant, is gratefully acknowledged [2015-6122].

Table of Contents

List of Tables

List of Figures

List of Variables

I	Nuclear spin quantum number
μ	Magnetic moment scalar
$\vec{\mu}$	Magnetic moment vector
B_0	Static magnetic field scalar
$\overrightarrow{B_0}$	Static magnetic field vector
B_1	Magnetic field of RF electromagnetic irradiation
E_m	Zeeman energy level
m	Quantum number for Z component of angular momentum
γ	Gyromagnetic ratio
$\hbar$	Reduced Planck constant
ΔE	Transition Energy
ω	Angular Frequency
T	Temperature
k	Boltzmann constant (1.38×10^{-23} J/K˚)
N_α	Number of Spins aligned with the field
N_β	Number of Spins against the field
N_S	Spin population characteristic of sample
M_0	Equilibrium sample magnetization
$\vec{M}$	Magnetization vector
M	Magnetization scalar
M_{xy}	Transverse magnetization
M_z	Longitudinal magnetization
$\vec{T}$	Torque vector
T	Torque scalar
t	Time
Δt	Time difference
J	Angular momentum
θ, φ	Angle of rotation
α	Flip angle
TR	Recovery time constant
90_x°	RF irradiation which rotates magnetization 90˚ about the x-axis
180_y°	RF irradiation which rotates magnetization 180˚ about the y-axis
PW_{90^o}	Duration of the 90_x° pulse
PW_{180^o}	Duration of the 180_y° pulse
τ	Dephasing time
T_2	Spin-spin decay time constant
$T_{2,eff}$	The experimental T_2, transverse signal lifetime, with diffusion contributions
$T_{2,intr}$	The intrinsic T_2

T_2^*	Effective transverse relaxation time with field inhomogeneity contribution
T_1	Longitudinal spin lattice relaxation time
n	Number of echoes acquired
R	Radius
h	Height
$\Delta_{1/2}$	Spectral linewidth
D	Diffusion coefficient
G	Magnetic field gradient
G_x	Magnetic field gradient oriented along the x-direction
T_E	Echo time (2τ)
ϕ	Phase shift
ϕ_{odd}	Phase shift of an odd echo
w	Flow behavioural index
m	Simplified behavioural index
v	Velocity
Q	Volume flux
r	Radial position within a glass-pipe
L	Length of pipe
Δp	Pressure drop
k	Fluid consistency
v_{avg}	Average velocity
v_{max}	Maximum velocity

List of Abbreviations

MR	Magnetic Resonance
MRI	Magnetic Resonance Imaging
RF	Radio Frequency
FID	Free-induction decay
SNR	Signal-to-Noise Ratio
CPMG	Carr-Purcell-Meiboom-Gill
Proteus	PROTon Embedded sUbmersible Sensor
1D	1-Dimensional
2D	2-Dimensional
Q-Factor	Quality-Factor
Re	Reynolds number

Chapter 1: Introduction

Magnetic Resonance (MR) dates back to Felix Bloch and Edward Purcell in 1946 [1,2]. They independently employed MR to characterize the properties of liquids and solids respectively. Bloch & Purcell determined that magnetic moments with non-zero spin atomic nuclei, ex. ^{1}H, absorb RF (Radio Frequency) energy when in the presence of an external magnetic field. The pair demonstrated that the absorption of the energy could be observed due to the precession of the nuclei about the polarizing magnetic field when in resonance with an RF excitation. Bloch & Purcell won the Nobel Prize in Physics in 1952. MR has since become a powerful means of studying the molecular structure and dynamics of matter in chemistry, physics, and medicine.

After the discovery of MR, the seminal work of Grannel & Mansfield [3] introduced the foundational principles of MRI (Magnetic Resonance Imaging). The emergence of MRI scanners in the field of medicine proved pivotal as a non-invasive means of imaging, offering major advantages over pre-existing X-ray technology. Closed, center-field, solenoid electromagnets were employed in the design of standard MRI scanners as the geometry permitted reasonable homogeneity and strong field strength in a substantial sample space, resulting in measurements of high sensitivity. Due to these advantages the centre-field design became a default in the advent of compact MR systems that are

generally applied for simple composition analysis, commonly referred to as portable MR.

Portable MR usually employs permanent magnets – which are a stark contrast to the superconducting magnets now commonly employed for MRI. Permanent magnet assemblies, compared to superconducting magnets, are light-weight and affordable in part because they tend to be much smaller. However, the permanent magnets themselves generally have a lower field strength and greater inhomogeneity. Depending on their purpose, MR magnets are typically generalized as magnets with sufficient field homogeneity for MR spectroscopy, imaging, and relaxometry, and magnets with lesser homogeneity, which are suitable for just relaxometry. Relaxometry is the study of relaxation times which characterize how spins equilibrate or decay following an excitation. Although MR relaxation measurements are possible in inhomogeneous fields the sample size, inhomogeneity, and RF excitation bandwidth limit their function.

Centre-field magnets are relatively common, however their application as a low-cost submersible sensor capable of relaxation measurements has not been extensively explored. Nor has the analysis of flowing fluids with a centre-field magnet would also have significant application to rheology. This work seeks to demonstrate a simple centre-field disk magnet design which optimizes sample volume, field strength and homogeneity, intended for relaxation studies. A quantitative design and measurement approach were taken to optimize the

signal-to-noise ratio (SNR) of the sensor for echo-train measurements. To remedy the disadvantages of a constrained sample space, the magnet was designed to be completely submerged in order for liquids to occupy the measurement volume. Success of the initial magnet design led to modifications that permitted analysis of laminar flowing fluids in a glass pipe.

Chapter 2 of this thesis is a general overview of MR theory. Chapter 3 is largely based on Ross et al. (2021), a manuscript accepted by the Journal of Magnetic Resonance entitled 'A Portable, Submersible, MR Sensor – The Proteus Magnet' [4]. Chapter 4 is largely based on a Ross et al. (2021) draft manuscript formatted for the Journal of Magnetic Resonance, entitled 'MR Measurement of Laminar Flow Employing a Proteus Magnet with Constant Magnetic Field Gradient'. Chapter 5 is the conclusion of the work and a discussion on future studies.

In this thesis we develop portable MR magnets and measurement concepts, Chapters 3 and 4, which are then illustrated with select MR measurement examples. The Proteus magnets of Chapters 3 and 4 are a significant advance in the state of the art and velocity measurements related to the examples of Chapter 4 have the potential to be revolutionary for rheology studies.

References

[1] Bloch, F. (1946). Nuclear induction. Physical Review, 70(7-8), 460.

[2] Purcell, E. M., Pound, R. V., & Bloembergen, N. (1946). Nuclear magnetic resonance absorption in hydrogen gas. Physical Review, 70(11-12), 986.

[3] Garroway, A. N., Grannell, P. K., & Mansfield, P. (1974). Image formation in NMR by a selective irradiative process. Journal of Physics C: Solid State Physics, 7(24), L457.

[4] Ross, M.M.B., Wilbur, G.W., Cano Barrita, P.F.J., Balcom, B.J. (2021), A Portable, Submersible, MR Sensor – The Proteus Magnet, J. Magn., Res 326, 106964.

Chapter 2: Introduction to Magnetic Resonance

2.1 Quantum Mechanical approach to Magnetic Resonance

Magnetic resonance (MR) is a phenomenon that depends on the natural properties of atomic particles and their nuclei. MR relies on the principles of quantum mechanics, as all particles possess the property of spin I, where I can be expressed as either 0, a half integer or integer, depending on the nucleus. Nuclei with non-zero spin possess magnetic moments $\vec{\mu}$ that are oriented randomly in the absence of a static field $\overrightarrow{B_0}$. In the presence of an applied magnetic field $\overrightarrow{B_0}$ $\vec{\mu}$ will partially align with the field and precess. This effect is analogous to the precession of a spinning top that is caused by the interaction of angular momentum and the earth's gravitational field [1,2] as shown in Figure 2.1.

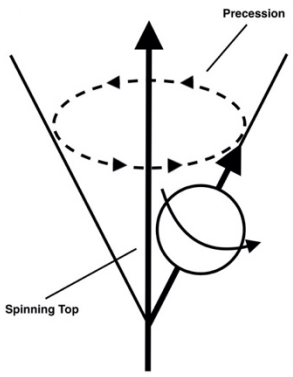

Figure 2.1 A precessing top whose precession is analogous to the precession of ^{1}H nuclei in a magnetic field

When a ^{1}H nuclei (spin 1/2) is in the presence of an applied external magnetic field, a phenomenon known as Zeeman splitting occurs where

magnetic moments take either one of two possible spin orientations. Zeeman splitting is illustrated in Figure 2.2.

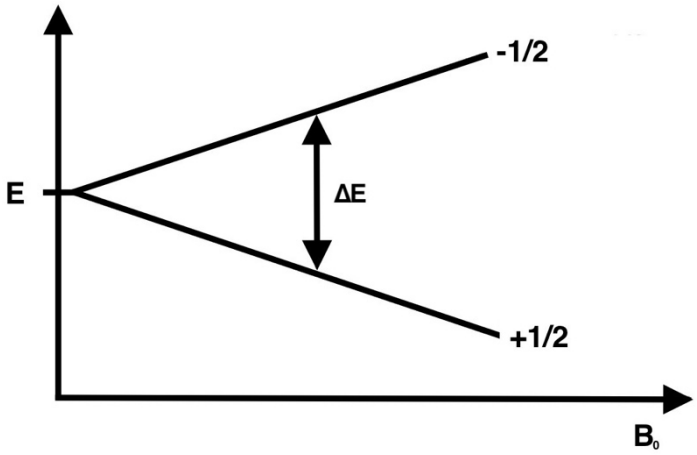

Figure 2.2 Zeeman energy levels of a ^{1}H nuclei in a static magnetic field B_0

Spins in different orientations will have different energy levels when interacting with the external field $\overrightarrow{B_0} = B_0\hat{z}$. The spin-up orientation will have lower energy and contain more spins than its anti-parallel counterpart, spin-down, where $E_m = -\gamma\hbar B_0 m$ for $m = \pm 1/2$. The energy difference between the $\pm 1/2$ spin states give a nonzero difference of

$$\Delta E = \gamma\hbar B_0 \qquad [2.1]$$

where γ and $\hbar$ are the gyromagnetic ratio and the reduced Planck constant respectively. γ is specific to ^{1}H (γ = 42.58 MHz/tesla). Recalling that $\Delta E = \hbar\omega$, where ω is the angular frequency of the magnetic moment, Eq. (2.1) can be rearranged to obtain the well-known Larmor equation

$$\omega = \gamma B_0. \quad [2.2]$$

The Larmor frequency is the rate of precession of a spin packet under the influence of a magnetic field. Additionally, the difference of spin population between the two states is related directly through their energy states. According to the Boltzmann relationship Eq. (2.3)

$$\frac{N_\alpha}{N_\beta} = exp\left(\frac{\Delta E}{kT}\right) \quad [2.3]$$

where T is temperature (K), k is the Boltzmann constant (1.38×10^{-23} J/K) and N_α and N_β are the number of spins pointing up and down respectively. A first-order approximation, $\Delta E \ll kT$, indicates there is a small excess number spins present within the lower-energy state. The unequal distribution between the two states is due to it being more probable spins take a lower-energy state as it has greater stability than the higher-energy state. Despite the small population difference between the two spin states, an observable macroscopic magnetization vector $\vec{M}$ is created by the spin system. The resulting bulk magnetization vector points exactly along the positive direction of z-axis. When at equilibrium its magnitude is

$$M = \left|\vec{M}\right| = \frac{\gamma^2 \hbar^2 B_0 N_s I(I+1)}{3kT} \quad [2.4]$$

for any spin-I system [1], where N_s is the total number of spins characteristic of the sample.

2.2 Classical Approach to Magnetic Resonance

The previously derived Larmor frequency demonstrates MR has solutions both quantum mechanically and classically. A magnetic moment $\vec{\mu}$ in a homogenous magnetic field $\overrightarrow{B_0}$ experiences a torque $\vec{T} = \vec{\mu} \times \overrightarrow{B_0}$ due to interaction with the applied field. Magnetic moments possess an intrinsic angular momentum *J* which causes the system to precess like a gyroscope with an angular frequency of ω, similar to the top in Figure 2.1. In a small period of time *t,* the angular momentum will change while maintaining the angle θ with the $\overrightarrow{B_0}$ oriented along the z-axis. After a period of Δ*t*, the angle of precession will be $\omega\Delta t$ and thus the time derivative of angular momentum can be stated as

$$\frac{dJ}{dt} = \omega J sin\theta \qquad [2.5]$$

Eq. (2.5) is also the torque of the system, or when expressed in terms of B_0,

$$\mathrm{T} = \mu B_0 sin\theta. \qquad [2.6]$$

Letting $\mu B_0 sin\theta = \omega J sin\theta$, and substituting $\frac{\mu}{J} = \gamma$, yields $\omega = \gamma B_0$, the same result as Eq. (2.2), proving the Larmor equation both classically and quantum mechanically.

2.3 Radiofrequency Excitation

Energy absorption in spin systems occurs when nuclei are irradiated with a burst of energy at the Larmor frequency. In MR this is generally performed through the application of RF energy invoked by RF coils. The RF coils also receive signal via electromagnetic induction. As a sample is positioned in a coil, a small sample magnetization is created that aligns with the magnetic field. The RF transmit coil then generates a pulse that produces a small magnetic field perpendicular to the static magnetic field B_0 [3]. The amplitude of the associated oscillating magnetic field is defined as B_1. When the RF energy is at resonance and is absorbed, spins from the higher-energy state are stimulated and move towards a lower-energy state. A similar effect occurs for the lower-energy-state spins. The B_1 field rotates net magnetization away from its alignment with the main magnetic field and the stronger, or longer, the RF pulse, the farther the magnetization will tilt or 'flip' [1,4]. When an applied B_1 is oriented along the transverse axis in the rotating frame the angle of precession will increase, resulting in the rotation of M towards the corresponding axis at a given flip-angle α. This is illustrated in Figure 2.3.

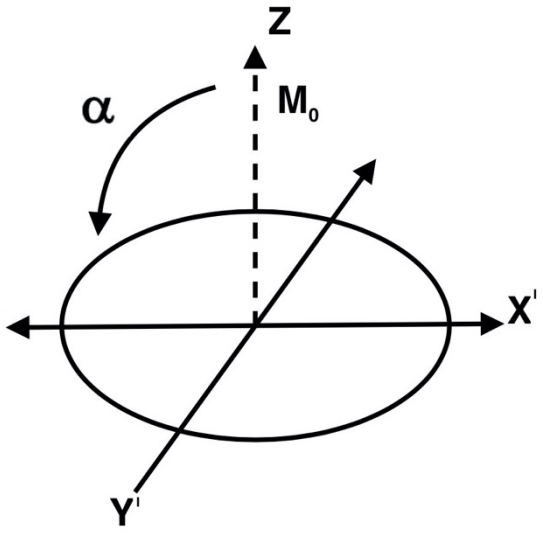

Figure 2.3 Magnetization vector, in a rotating frame of reference, rotated into the transverse plane, with an angle of rotation α

The net magnetization within the Cartesian plane can thus be described as rotating around the z-axis by

$$\vec{M} = M_0 \begin{bmatrix} sin\,\alpha\, sin\,(\omega t + \varphi) \\ sin\,\alpha\, cos\,(\omega t + \varphi) \\ cos\,\alpha \end{bmatrix} \quad [2.7]$$

where φ is the angle of rotation along the z-axis and M_0 is the initial magnetization. 90°_{x} and 180°_{y} RF pulses can be applied to excite the spins. The RF receiver coil detects the precession resulting in an induced electric current via electromagnetic induction. The induced voltage is the observable MR signal and represents the oscillating magnetization within a sample.

2.4 Relaxation

The application of the RF pulse prompts transitions between energy states. This dictates that energy must be introduced into the spin system. Procedurally, the spin energy of the nuclei dissipates resulting in the return of excited spins to equilibrium. The return to equilibrium following an RF excitation is governed by time constants T_1, T_2, and T_2^*.

2.4.1 T_1 Relaxation

The longitudinal spin relaxation time, T_1, is the time constant that describes the process of spin-lattice relaxation which results in recovery of the longitudinal magnetization. Spin-lattice relaxation is indicative of the energy transfer between spins and the lattice. The lattice is defined as the thermal reservoir in which the spins are localized, and the coupling interaction between the two. The rate at which magnetization reorients with the applied magnetic field can be as short as a few milliseconds or as long as several of seconds. The expression for the $M_z(\tau)$ recovery along the z-axis after a 90°_x RF pulse is described in Eq. [2.8]:

$$M_z(\tau) = M_z(0)\left(1 - exp\left(-\frac{\tau}{T_1}\right)\right). \qquad [2.8]$$

2.4.2 T_2 and T_2^* Relaxation

The T_2 decay constant, referred to as the spin-spin relaxation lifetime, describes the rate at which transverse magnetization's phase coherence is lost within the spin system. The loss of coherence is due to interactions between neighboring spins and is indicative of the sample's structure and dynamics as well as the applied static magnetic field. If mono-exponential decay the magnetization decay is expressed as

$$M_{xy}(\tau) = M_{xy}(0)exp\ (-\frac{\tau}{T_2}) \quad [2.9]$$

where τ time has passed since the RF pulse was applied, and $M_{xy}(0)$ is the initial excited transverse magnetization. Decay may be multiexponential.

Spin-spin interaction is not the only factor affecting the de-phasing of spins. Field inhomogeneity can also result in a loss of coherence and increase the rate of transverse decay. T_2^* – or the effective spin-spin relaxation time – includes a contribution from magnetic field inhomogeneities ΔB_0, described in Eq. [2.10]

$$\frac{1}{T_{2^*}} = \frac{1}{T_2} + \gamma\Delta B_0. \quad [2.10]$$

2.5 Carr-Purcell-Meiboom-Gill T_2 Measurement

Relaxometers, the MR instruments which perform relaxation-based measurements, employ a Carr-Purcell-Meiboom-Gill (CPMG) RF pulse sequence [5-7] which can be described as follows

$$90^{\circ}_{x} - \left(\tau - 180^{\circ}_{y} - \tau - echo\right)_{n}. \qquad [2.11]$$

τ is the dephasing time and *n* the number of echoes generated. After applying the initial 90°_{x} RF pulse, the system dephases within a short time interval τ and then refocuses with a 180°_{y}, rotating the sample magnetization in the transverse plane. This produces a spin echo. Repeating the process can generate a series of echoes. Figure 2.4 illustrates this pulse sequence for the acquisition of multiple echoes.

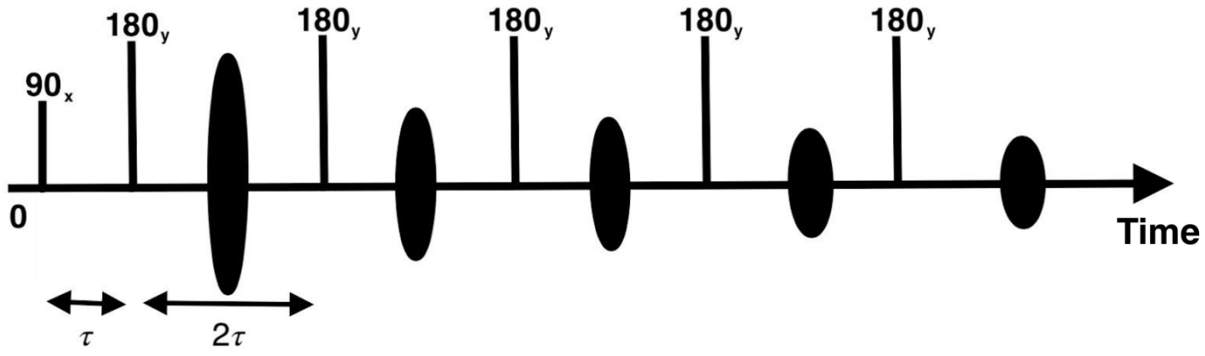

Figure 2.4 The CPMG pulse sequence, a 90_{x}° pulse followed by a series of n 180_{y}° pulses refocuses the magnetization to obtain *n* echoes.

While the CPMG method allows for spins to refocus, removing the effect of static field inhomogeneity, there is an additional unavoidable attenuation due to diffusion and the intrinsic spin-spin relaxation.

2.6 Diffusion Measurements in Inhomogeneous Fields

The experimental T_2, or $T_{2,eff}$, is influenced by diffusion effects due to the underlying magnetic field gradients [8-11] embodied in the intrinsic time decay $T_{2,intr}$, expressed as

$$\frac{1}{T_{2,eff}} = \frac{1}{T_{2,intr}} + \frac{D(\gamma G T_E)^2}{12} \qquad [2.12]$$

where D is the diffusion coefficient, G is the gradient, and T_E is the echo time. The attenuation of observable signal by molecular diffusion through magnetic field gradients is important for portable MR since the magnetic field employed is usually inhomogeneous in the measurement volume, with a distribution of local gradients. The amplitude of G can be due to imperfections in the magnet or a deliberate design choice to impose a macroscopic constant gradient. By performing several CPMG measurements with varying T_E, one can obtain a straight-line fitting from the inversed $T_{2,eff}$ versus T_E^2 to obtain the diffusion constant, provided G is known.

2.7 MR Flow Measurements

2.7.1 Introduction to MR Flow Measurements

Performing a CPMG measurement of a flowing fluid results in an echo rephasing phenomenon that encodes velocity in the phase shift of the flow [12]. The behaviour of this phenomenon can best be described as follows: observing the intensities of the first two echoes, the second should naturally be less intense than the first due to T_2 relaxation and diffusion. However, in flow measurements the intensity of the second echo is often much greater than the first. This holds true for the entirety of an *n*-length echo train, as the amplitude of all even echoes will be greater than the odd echo which immediately preceded it [13]. Figure 2.5 illustrates the alteration of real and imaginary components of echoes acquired through CPMG measurement when flow occurs.

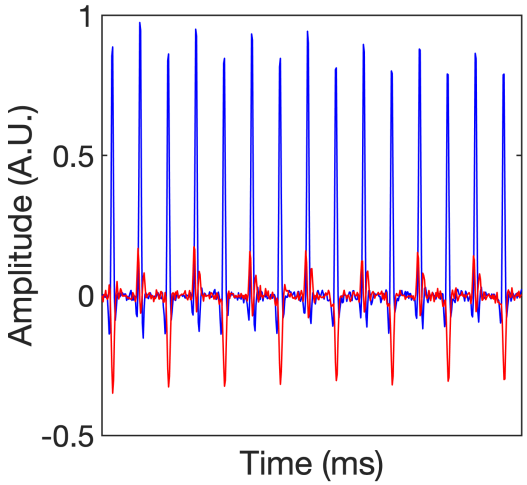

Figure 2.5 CPMG echo train measurement of $CuSO_4$ doped tap water undergoing laminar flow. The real and imaginary signal is represented by blue and red respectively. The odd echoes undergo a phase shift compared to even echoes.

The odd echo phase shift effect is due to an incomplete rephasing of sample magnetization by the first $180_y°$ RF pulse in Eq. (2.11), which diminishes the overall intensity of the odd spin echo. After the application of a second $180_y°$ of rotation, re-phasing is complete, generating a complete even echo, however the phase shift remains encoded in the odd echo. The signal intensity remains attenuated due T_2 relaxation and diffusion, however the phase shift encoded in the odd echoes is unaffected. The phase shift can be calculated through the phase angle between the real and imaginary components of the echo.

2.7.2 MR Phase Shift Measurements of Flow

A phase shift occurs for odd echoes in the CPMG measurement when fluid flows in the direction of a constant gradient G_x. For constant velocity, the phase accumulation ϕ can be expressed as Eq. (2.13), where γ is the gyromagnetic ratio and v is velocity [13].

$$\phi = \gamma v \int G_x(t)\, tdt = \gamma v G_x \int tdt \qquad [2.13]$$

During CPMG measurement, the MR signal phase at the $180_y°$ pulse will be reversed. For the first odd echo, phase accumulation can be calculated as Eq. (2.14).

$$\phi_{odd} = -\gamma v G_x \int_0^{\tau} tdt + \gamma v G_x \int_{\tau}^{2\tau} tdt = \gamma v_{avg} G_x \tau^2 \qquad [2.14]$$

The phase shift can be calculated through the phase angle between the real and imaginary components of the echo, as seen in Figure 2.5, to determine the average velocity of the flow provided a constant gradient is present and is oriented in the direction of flow. Note this equation is for flow along one streamline in the sample. Other streamlines may have different velocities.

References

[1] Liang, Z. P., & Lauterbur, P. C. (2000). Principles of Magnetic Resonance imaging: a signal processing perspective. SPIE Optical Engineering Press.

[2] Callaghan, P. T. (1993). Principles of nuclear magnetic resonance microscopy. Oxford University Press on Demand.

[3] Hoult, D. I. (1978). The NMR receiver: a description and analysis of design. Progress in Nuclear Magnetic Resonance Spectroscopy, 12(1), 41-77.

[4] Fukushima, E. (2018). Experimental pulse NMR: a nuts and bolts approach. CRC Press.

[5] Meiboom, S., & Gill, D. (1958). Modified spin-echo method for measuring nuclear relaxation times. Review of scientific instruments, 29(8), 688-691.

[6] Hahn, E. L. (1950). Spin echoes. Physical review, 80(4), 580.

[7] Carr, H. Y., & Purcell, E. M. (1954). Effects of diffusion on free precession in nuclear magnetic resonance experiments. Physical review, 94(3), 630.

[8] Hürlimann, M. D., & Venkataramanan, L. (2002). Quantitative measurement of two-dimensional distribution functions of diffusion and relaxation in grossly inhomogeneous fields. Journal of Magnetic Resonance, 157(1), 31-42.

[9] Rata, D. G., Casanova, F., Perlo, J., Demco, D. E., & Blümich, B. (2006). Self-diffusion measurements by a mobile single-sided NMR sensor with improved magnetic field gradient. Journal of Magnetic Resonance, 180(2), 229-235.

[10] Hürlimann, M. D. (2001). Diffusion and relaxation effects in general stray field NMR experiments. Journal of Magnetic Resonance, 148(2), 367-378.

[11] Hürlimann, M. D. (2007). Encoding of diffusion and T_1 in the CPMG echo shape: Single-shot D and T_1 measurements in grossly inhomogeneous fields. Journal of Magnetic Resonance, 184(1), 114-129.

[12] Pope, J. M., & Yao, S. (1993). Quantitative NMR imaging of flow. Concepts in Magnetic Resonance, 5(4), 281-302.

[13] Nishimura, D.G. (2010), Principles of Magnetic Resonance Imaging, 23–98 & 203–212.

Chapter 3: A Portable, Submersible, MR Sensor – The Proteus Magnet

This chapter is largely based on the paper “A Portable, Submersible, MR Sensor – The Proteus Magnet”, published in the Journal of Magnetic Resonance [1]. It describes the construction and application of the submersible, centre-field, Proteus magnet intended for determination of fluid composition studies of various samples.

The format of references in this chapter follows that of the original paper.

3.1 Introduction

Portable Magnetic Resonance (MR) is an emerging field that has introduced MR to a broad range of industrial applications [2,3]. Portable MR instruments are commonly based on strong permanent magnets, with a static field homogeneity that is insufficient for spectroscopy. Multiple sensors have been introduced over the past two decades, including the single-sided NMR-MOUSE, 3-Magnet Array, and the Barrel Magnet – all of which have been employed, for a variety of measurements, by research groups other than the inventors [4-7]. Enclosed magnets result in a more uniform static field and naturally support enclosing RF probes that have higher sensitivity than single-sided systems. Blümich and colleagues have developed enclosed magnets based on a Halbach geometry. The Halbach design, combined with techniques

for shimming the static field, and passive cancellation of the temperature coefficient of the permanent magnets, permits spectroscopy [8,9].

In this paper we introduce the Proteus (PROTon Embedded sUbmersible Sensor) magnet, a palm-sized enclosed submersible MR sensor capable of elementary relaxation-based measurements. We seek the benefits of a simple enclosed magnet topology with the attendant SNR advantage, but do not aspire to the homogeneity required for spectroscopy. Bulk measurements of interest include CPMG, T_1, $T_1 - T_2$, self-diffusion, and $D - T_2$ [10-14]. Simple motion encoding with the natural inhomogeneity of these magnets is a major design advantage, achieved passively. We have named this class of magnets Proteus magnets after the Greek god of oceans and rivers, as well as in honour of the submersible from the movie 'The Fantastic Voyage'. The Proteus magnet is portable, weighing under 0.15 kg. Equipped with a simple console and RF amplifier the Proteus magnet forms the heart of an MR relaxometer that may be readily deployed outside of a dedicated research laboratory.

The Proteus magnet is simple to construct, as the static field within the enclosed structure is created with a pair of low-cost, nickel-coated N52 grade NdFeB disk magnets – which can be readily acquired from a variety of vendors. The RF probe and shield are placed between the NdFeB magnets, with North and South poles aligned. To permit submersion, the magnets and probe are coated in epoxy to limit fluid penetration. The natural linewidth of the Proteus

magnet is too broad for spectroscopy; however, it remains suitable for relaxation-based measurements.

The Proteus magnet is related to previous sensor designs which also utilized a pair of permanent dipole magnets - including iterations which were applied to measure evaporable water in concrete samples and water in constructed marshland habitats [15,16]. Similar designs also include the sacrificial embedded single-sided magnet and lab-on-a-chip MR system [17,18]. The Proteus magnets do not emphasize miniaturization of the magnet and console. The objective of the Proteus magnet is a simple deployable sensor which can be readily utilized outside of a dedicated research laboratory. We employ an analytical approach to maximize the region of homogeneous field, to improve the sample volume and consequentially the signal-to-noise ratio (SNR).

3.2 Theory

The magnetic field strength of an individual disk magnet at an arbitrary distance z above its center can be derived similarly to the field above any circular loop of conductor with steady current [19]. The individual disk magnet has a remanence B_r, a thickness h, and a radius R. By integrating along the central axis an expression for the magnetic field in surrounding space can be readily obtained. Introducing a second identical magnet, displaced distance d from the first, generates a net field that has reasonable homogeneity in a

macroscopic volume between the individual magnets. By the principle of superposition, the net field strength of the two disk magnets can be expressed as Eq. (3.1).

$$B_z(x,z) = \frac{B_r}{4}\left(\frac{\frac{d}{2}+z+h}{\sqrt{(R+x)^2+\left(\frac{d}{2}+z+h\right)^2}} - \frac{\frac{d}{2}+z}{\sqrt{(R+x)^2+\left(\frac{d}{2}+z\right)^2}} + \frac{\frac{d}{2}+z+h}{\sqrt{(R-x)^2+\left(\frac{d}{2}+z+h\right)^2}} - \frac{\frac{d}{2}+z}{\sqrt{(R-x)^2+\left(\frac{d}{2}+z\right)^2}} + \frac{\frac{d}{2}-z+h}{\sqrt{(R+x)^2+\left(\frac{d}{2}-z+h\right)^2}} - \frac{\frac{d}{2}-z}{\sqrt{(R+x)^2+\left(\frac{d}{2}-z\right)^2}} + \frac{\frac{d}{2}-z+h}{\sqrt{(R-x)^2+\left(\frac{d}{2}-z+h\right)^2}} - \frac{\frac{d}{2}-z}{\sqrt{(R-x)^2+\left(\frac{d}{2}-z\right)^2}} \right) \quad [3.1]$$

Due to the radial symmetry of the disk magnets, Eq. (3.1) permits one to calculate the $B_z(y,z)$ component of field by substituting *y* for *x* in the equation and $B_z(x,y)$ through calculations with Z constant. Eq. (3.1) enables simulation of the magnetic field for any arbitrary disk magnet combination.

3.3 Experimental

3.3.1 Sensor Construction

A pair of K&J Magnetics (Pipersville, PA) N52 grade NdFeB disk magnets – 31.75 mm in diameter and 6.35 mm in thickness – were separated by a rigid printed circuit (PC) board box. This combination of magnets generated a

reasonably uniform 0.4 T field in the measurement volume. The exterior walls of the box were fabricated from 0.8 mm thick double clad PC board. The top and bottom surfaces were fabricated from 0.4 mm thick double clad PC board. The outer dimensions of the box were 31.75 mm × 48 mm × 10 mm. The interior edges were soldered, ensuring that all pieces were connected both mechanically and electrically.

A rectangular solenoid was utilized as the RF probe. A rectangular solenoid was favoured as it possessed approximately the same sensitivity as a square or circular solenoid but better matched the available sample space [20]. The RF probe former was 3D printed from polylactic acid. The RF coil was comprised of five turns of 0.8 mm magnet wire, over a distance of 5 mm, wrapped on the Teflon tape covering the former. The probe former and Teflon tape were removed by gentle heating once the RF probe was fabricated. The RF probe was connected to an external tuning and matching circuit which provided the sensor a tuning range of ± 2 MHz.

The RF coax probe connection was grounded to the interior and exterior of the PC board box. When grounded, the PC board surrounding the probe functioned as an RF shield. The box was filled with an epoxy resin, Loctite EA M-31CL (Düsseldorf, Germany), to maintain rigidity once the magnets were positioned. The epoxy was cured over 24 hours. The entire box, with magnets in place, were coated with the same epoxy and again left to cure, to ensure the

Proteus magnet was impermeable to fluids. Figure 3.1 is a photo of the completed 0.4 T Proteus magnet.

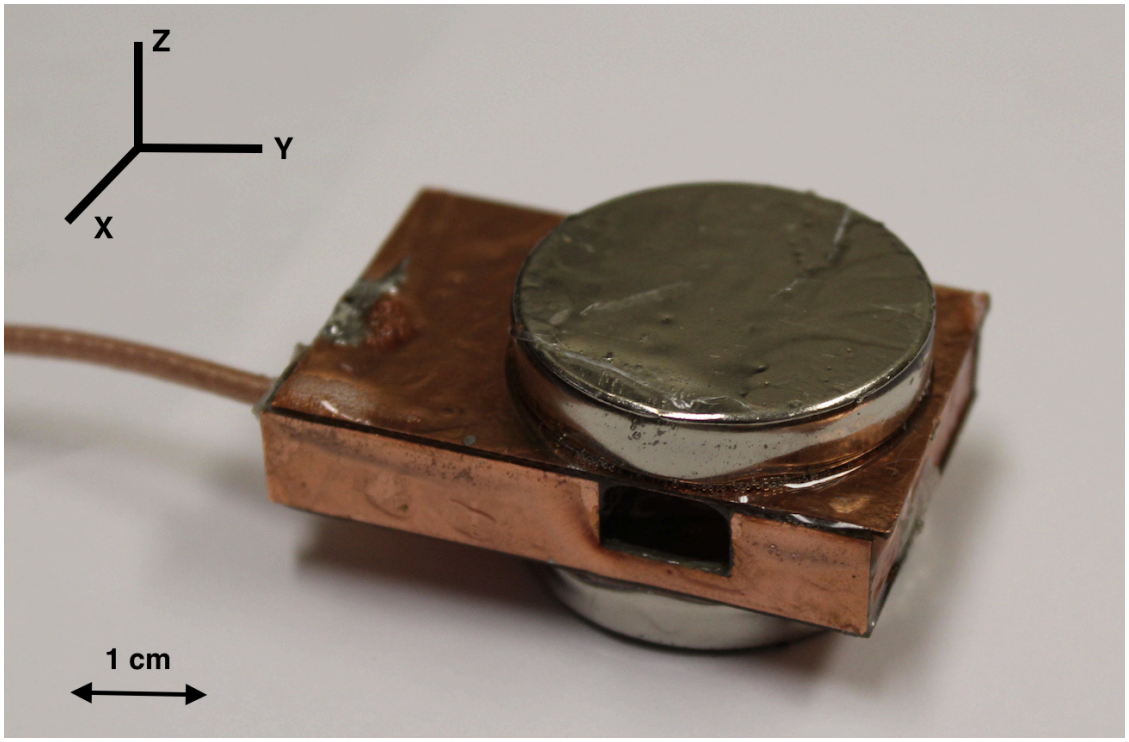

Figure 3.1 Photo of the prototype 0.4 T Proteus magnet. Two N52 disk magnets were separated by a 10 mm gap with the RF probe placed within the homogeneous field region. The Proteus magnet is coated in epoxy to allow for submersion in liquid samples.

3.3.2 Hardware Setup

3.3.2.1 Magnetic Field Plots

Field plots were obtained with a LakeShore (Westerville, OH) 450 Gaussmeter translated by a multi-axis translational stage (Thorlabs, Newton, NJ). Only $B_z(x,0)$ was measured due to the size and directional limitations of the

Gaussmeter probe. Magnetic fields $B_z(0,z)$, $B_z(x,0)$, $B_z(x,z)$, and $B_z(x,y)$ were calculated.

3.3.2.2 Console and RF Circuitry

The RF probe was attached to a TecMag (Houston, TX) Transcoupler II with a λ/4 cable via BNC connectors. The transcoupler was joined to a Tomco Technologies (Stepney, Australia) 250-Watt RF amplifier and a L3 Nard-MITEQ (Hauppauge, NY) 0.7 – 200 MHz preamplifier with a Mini-Circuits (Toronto, Ontario) 30 MHz low-band-pass filter. The system was run by a TecMag LapNMR console.

3.3.3 Measurement Details

Measurements were undertaken with the Proteus magnet immersed in solution, and with liquid samples held in a small rubber vessel inserted into the RF probe. The signal from the rubber was significantly less than that of the liquids measured. A filter width of 0.1 MHz and dwell time of 5 μs were employed in each measurement. The Proteus magnet was not temperature controlled. All measurements were conducted at ambient temperature. A two-dimensional Fast Laplace Inversion algorithm with Tikhonov regularization was employed for $T_1 - T_2$ and $D - T_2$ correlation determination [12]. The inversion was undertaken with code kindly provided by Schlumberger.

The measurement SNR was calculated as the ratio between the average magnitude of the first three echoes in a CPMG measurement divided by the standard deviation of the last ten echoes of the measurement once signal had fully decayed. The PW_{90^o} and PW_{180^o} were 4.1 μs. The 90_x° pulse was attenuated by a factor of 1/2 in CPMG measurements. Table 3.1 details the measurement parameters employed to determine the SNR from a Staedtler Mars elastomer eraser (Nuremberg, Germany) which was employed as a phantom.

Cod Liver Oil (Life Brand, Toronto, ON), was measured with a bulk CPMG measurement, T_E = 300 μs, to determine T_2. 1024 echoes were acquired with 8 averages, recovery time TR = 500 ms, for a total measurement time 5 s. T_1 was determined through evaluating the second echo in a saturation-recovery CPMG measurement. The T_1 parameter was determined with 11 saturation-recovery delays and 32 averages, for a total measurement time of 90 s.

The average-gradient G of the Proteus magnet was determined by measuring self-diffusion in a distilled water sample with known D = 2.023 x 10^{-5} cm^2/sec at ambient temperature [21]. CPMG measurements with T_E's of 400,1200,1600,2600, and 3000 μs were undertaken with a minimum of 512 echoes. The decay constant for each echo train was determined after 8 averages. The total experimental time was 3.5 min.

The Proteus magnet was used to perform a $T_1 - T_2$ relaxation correlation measurement of a simple mixture composed of a 60% by mass sucrose solution in distilled water. The $T_1 - T_2$ measurement employed 11 saturation-recovery delays, 4 averages, T_E = 300 μs, 1024 echoes, and TR = 4 s. The regularization parameter α = 1 for inversion. Complete measurement required 5 min.

A $D - T_2$ measurement of the same sucrose solution was also performed, employing a diffusion encoding pulse sequence described by Hürlimann [22]. The D – T_2 measurement had a variable first echo with T_E's of 40, 120, 400, 720, 1050, 1400, 1800, 2300, 2600, 3200 μs, followed by an echo train with fixed T_E of 300 μs, TR = 4 s, 1024 echoes, and 8 averages. The regularization parameter was α = 0.1 for inversion. The measurement required 5 min.

Depth-resolved measurements employed cod liver oil and distilled water doped with 0.3% $CuSO_4$ poured into a 1 L glass beaker. Each fluid phase occupied approximately half the volume of the container. Water, with a higher density occupied the lower half of the beaker. The Proteus magnet was submerged in the vessel at variable depth. Unique $T_1 - T_2$ measurements were undertaken in each layer. The cod liver oil and water layers were each measured in 3 min with 4 averages, 1024 echoes, T_E = 300 μs, TR = 1 s, and 8 identical saturation-recovery delays. The regularization parameter was α = 1.

The Proteus magnet was employed to perform a $T_1 - T_2$ relaxation correlation measurement of a 99% isopropyl rubbing alcohol (RW Consumer Products, St. Albert, AB) and 70% isopropyl skin cleanser (Laboratoire Atlas Inc., Montreal, QC). The $T_1 - T_2$ measurement employed 12 saturation-recovery delays, 4 averages, T_E = 300 μs, 1024 echoes, and TR = 5 s. The regularization parameter for the 99% solution regularization was α = 1. The regularization parameter for the 70% solution was α = 0.1. Each complete measurement required 6 min.

3.4 Results and Discussion

3.4.1 Field Plots and Measurement Volume

Figures 3.2a and 3.2b depict the experimental and calculated field distributions $Bz(x,0)$ and the calculated field distribution $B_z(0,z)$ of the Proteus magnet. Figures 3.2c and 3.2d are contour plots of the $B_z(x,y)$ and $B_z(x,z)$ respectively. Eq. (3.1) was employed to simulate the field distributions for a variety of magnet separations. The optimum separation, based on a compromise of measurement volume and field homogeneity was determined to be 10 mm. The calculated and measured field distribution for $B_z(x,0)$ agree very well, with a flat field profile, giving a B_z value of 0.4 T in the centre of the Proteus magnet. The calculated field $B_z(0,z)$ is consistent with the measured field in the sensitive spot and yields a uniform field in the z direction. A 5 x 10 x 7 mm rectangular RF probe was constructed to match the chosen region. The ID of

the RF probe was 7 mm in the z direction. The length of the RF probe was 5 mm in the x direction. The measurement volume was 350 mm^3. The magnetic field of 0.4 T corresponds to a resonance frequency of 17 MHz for ^1H.

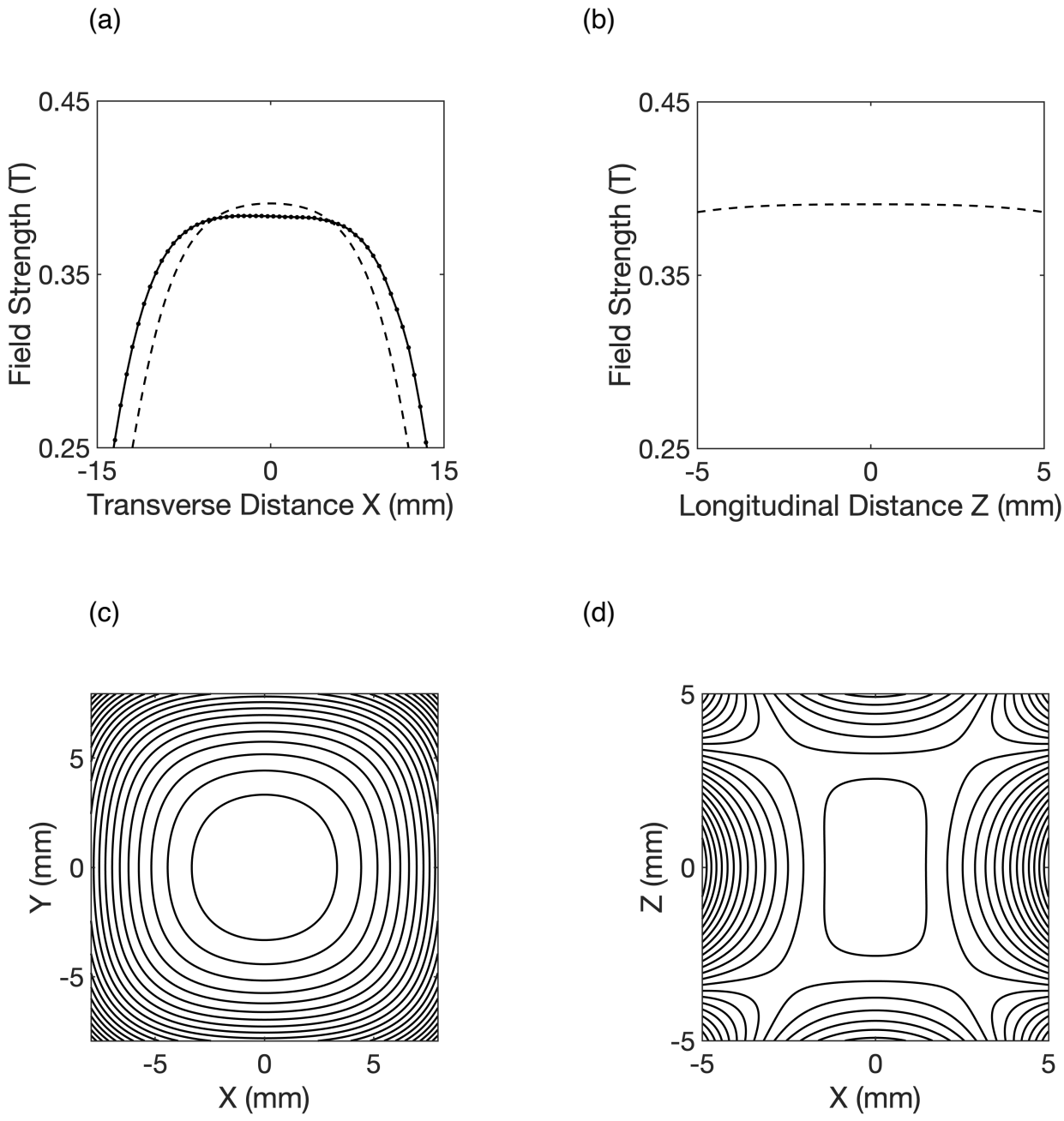

Figure 3.2 Field plots of two N52 disk magnets - 31.75 mm in diameter and 6.35 mm in thickness - separated by 10 mm. The field strength was measured from the center of the sample volume to the edge. The RF probe, 5 mm in length, was centered about the origin. Calculated (--) results were determined using Eq. (3.1). (**a**) The calculated $B_z(x,0)$ distribution of the Proteus magnet, and the experimental $B_z(x,0)$ distribution. Experimental (•) results were acquired employing a Gaussmeter traversed through the magnet cavity. (**b**) The $B_z(0,z)$ distribution of the Proteus magnet calculated from Eq. (1). The $B_z(0,z)$ was not measured due to finite size of the Gaussmeter probe. The z range is limited to the magnet spacing. (**c**) The $B_z(x,y)$ distribution of the Proteus magnet at z = 0. The centre point field is 0.4 T, the contour intervals are 0.5 mT. (**d**) The $B_z(x,z)$ distribution of the Proteus magnet at y = 0. The centre point field is 0.4 Tesla, the contour intervals are 0.5 mT. The displayed range of z is limited to the magnet separation.

The Proteus magnet is capable of measurements within ± 20 °C of ambient temperature. A temperature change of ± 5 °C alters the magnetic field by 0.1 MHz. Simulations of the field topology show that an increase in temperature results in a lower field strength and a broader sensitive spot, while a decrease in temperature has the converse effect. The RF coil implemented in the Proteus magnet will probe the sensitive spot, regardless of temperature, and would only require tuning to match the new field. The Proteus magnet has sufficient homogeneity that an FID may be observed in simple pulse acquire measurements. Through acquisition of the FID the MR resonance frequency can be determined. The Proteus magnet can function over a wide range of temperatures. As an immersible sensor it is designed, passively, to equilibrate to the temperature of the fluid to be measured. The ability to measure samples in a wide temperature range is critical to this strategy.

3.4.2 Magnet and RF Coil

Fukushima's method was employed to calculate the PW_{90^o} from the known RF power, Q-factor, measurement volume, and RF frequency [22]. The expected PW_{90^o} value with 29 dB of attenuation, a Q-factor of 62, a volume of 350 mm^3, and 17 MHz frequency was 2.8 μs. The PW_{90^o} was experimentally determined, with a quadrature-echo measurement of the elastomer phantom, to be 4.1 μs. The SNR for the elastomer phantom, acquired with a CPMG measurement, was 19.9 for a 9 s measurement as reported in Table 3.1. The T_2

decay constant was 4.7 milliseconds. To ascertain the contribution of cured epoxy MR signal, a CPMG measurement with parameters set to detect a liquid sample was performed employing an empty Proteus magnet. With no distinguishable signal observed from the empty probe, it was concluded that the signal from the epoxy was not seriously influencing our measurements.

Frequency (MHz)	Filter Width (MHz)	PW_{90^o} (μs)	Dwell-time (μs)	No. of Scans	Echo Time (μs)	Repetition Time (ms)	RF Power (Watts)	Acquisition Time (s)
17	0.1	4.1	5	16	200	500	8.8	9

Table 3.1: CPMG and quadrature-echo sequence parameters to determine the sensitivity and PW_{90^o} of the elastomer phantom.

The RF probe deadtime was 10 μs. The field inhomogeneity was determined from the spectral line-width ($\Delta_{1/2}$) of an individual echo obtained from the elastomer phantom. The $\Delta_{1/2}$ was 12.7 kHz with a T_2^* of 25 μs determined from the echo rise and fall. The linewidth and T_2^* were confirmed with a separate free-induction decay measurement. The field homogeneity of the Proteus magnet, based on MR measurement was thus determined to be 7 parts in 10,000, which is 700 ppm.

3.4.3 Average Gradient

The Proteus magnet, being an enclosed magnet is naturally more homogeneous in terms of field than a single sided sensor. A homogeneity of 700

ppm in the measurement volume is good for relaxometry but insufficient for spectroscopy. In keeping with the ethos of the Proteus magnet no magnet shimming was employed. The naturally occurring field was thus inhomogeneous, but with a well-defined average gradient that results in diffusive attenuation of a CPMG echo train [23]. Using a sample of distilled water, the average gradient of the 17 MHz Proteus magnet was determined through this diffusion effect. Eq. 3.2 describes the experimental decay constant in a CPMG echo train and its relation to the gradient $\langle G \rangle$, diffusion coefficient D, and echo time T_E [13].

$$\frac{1}{T_{2,\text{effective}}} = \frac{1}{T_{2,\text{intrinsic}}} + \frac{D(\gamma\langle G\rangle T_E)^2}{12} \qquad [3.2]$$

Figure 3.3 shows the reciprocal of the exponential decay constant plotted versus the square of the echo time for five individual CPMG decays. The average gradient was determined from the slope of the plot in Figure 3.3 employing a known water self-diffusion coefficient. The average gradient was 0.98 T/m. We speak of an average gradient in the measurement volume because there is no well-defined macroscopic gradient. The straight-line relationship of Figure 3.3 does however suggest a well-defined and well-behaved diffusive attenuation and therefore a well-defined average gradient.

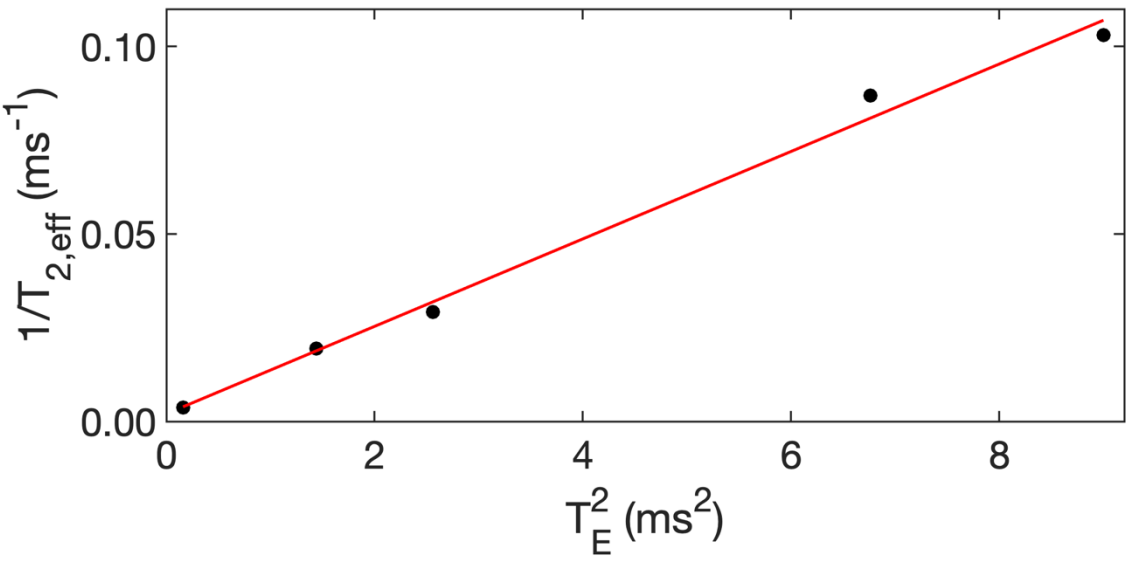

Figure 3.3 Plot of effective $1/T_2$ vs. T_E^2. The average gradient for the Proteus Magnet was $\langle G \rangle$ = 0.985 T/m. $\langle G \rangle$ was determined using distilled water which has a known self-diffusion coefficient of D = 2.023 x 10^{-5} cm^2/sec at 20˚C. With known $\langle G \rangle$ the same measurement could be employed to measure D in an unknown sample.

The average gradient is associated with local variation of the field in the sample space. If the gradient were constant and macroscopic, traversing the full sample space, the field homogeneity would be dramatically less, as low as 2 parts per 100. Employing Eq. 3.1 we calculated the spatial variation of the longitudinal field over distance scales somewhat larger than the characteristic diffusion length. The resulting grid of local magnetic field gradients were combined into a histogram and the average gradient determined (suppressing gradient sign). The average gradient was determined to be 1.3 T/m within the sensitive spot. The simulated average gradient is larger than the gradient measured experimentally, 0.98 T/m, via a diffusion experiment. Given the nature

of the comparison the agreement is pleasing. We note as well that the field plot of Figure 3.2a shows the measured field has less spatial variation than suggested by simulation. A well-behaved average magnetic field gradient $\langle G \rangle$ will permit the variable echo time CPMG measurement to be used to determine molecular self-diffusion in unknown solution samples.

3.4.4 T_1 and T_2 Measurement

One of the most useful portable MR measurements is a bulk CPMG. To test the sensitivity of the prototype Proteus magnet we undertook bulk T_2 measurement of a cod liver oil sample. Cod liver oil is an ideal test liquid [24,25] since as a viscous oil it has a short T_1 permitting rapid signal averaging.

Figure 3.4a shows the results of a CPMG measurement of the cod liver oil sample. The CPMG measurement had a SNR of 22 with 8 signal averages acquired in 5 seconds. The raw sensitivity of the Proteus magnet is such that single shot CPMG decays are a reasonable prospect. The CPMG T_2 decay was fit to a mono-exponentially decaying function and T_2 was determined to be 106 ms.

Figure 3.4b shows the results of a saturation recovery T_1 measurement of the cod liver oil sample. The T_1 was single exponential with eleven saturation recovery intervals. The T_1 fit gave a value of 120 ms. The T_1 measurement was

based on magnitude of the amplitude of the second echo in a CPMG echo train as longitudinal magnetization recovers from saturation. This certainly suggests a $T_1 - T_2$ relaxation correlation measurement has general utility with the Proteus magnet.

(a)

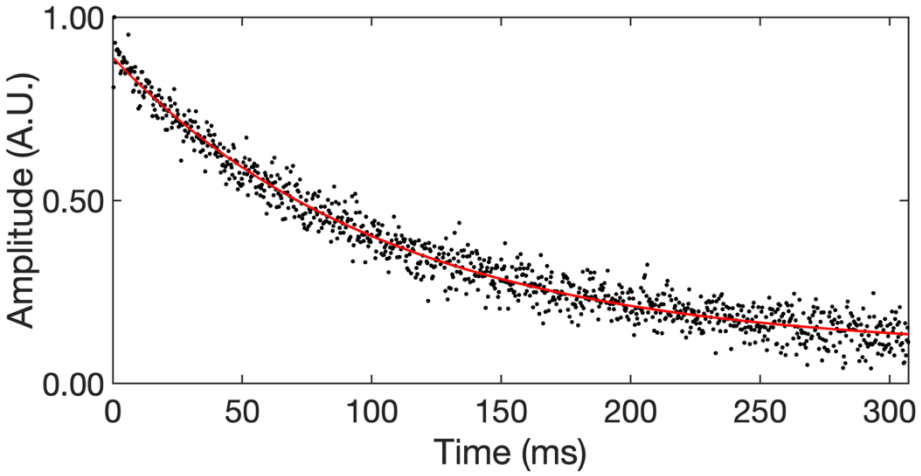

(b)

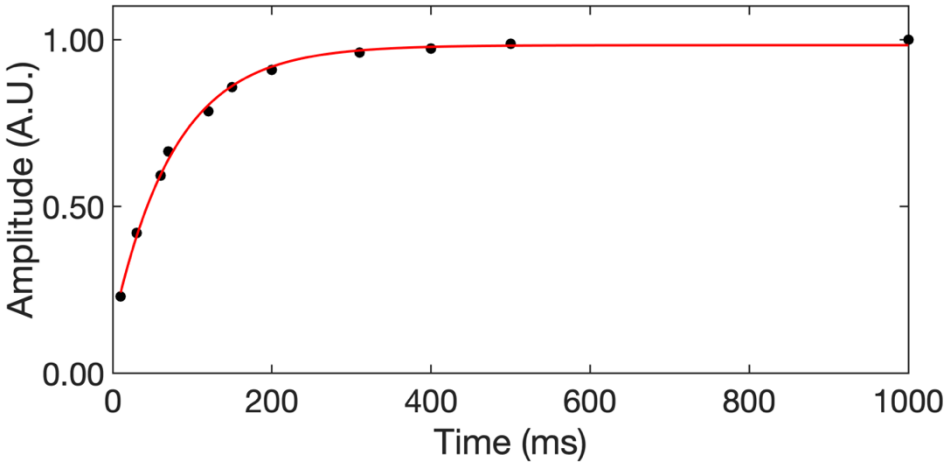

Figure 3.4 Normalized bulk T_2 and T_1 CPMG measurements of a cod liver oil test sample (**a**) The T_2 was determined to be 106 ms. The measurement required 5 s. The SNR was 22. (**b**) The T_1 measurement of the cod liver oil. The T_1 was determined to be 120 ms.

3.4.5 $T_1 - T_2$ Measurement

$T_1 - T_2$ measurements have broad applicability to measurements of liquid composition and have proven invaluable in determining wettability of porous media [12,26-28]. The $T_1 - T_2$ measurement requires only a simple modification of the bulk saturation recovery T_1 measurement described in the previous section. Given the putative utility of the Proteus magnets for measuring liquid composition we measured a model sucrose solution with a $T_1 - T_2$ measurement.

$T_1 - T_2$ measurement was undertaken on a 60% by mass sucrose solution. Two peaks are readily observed in the $T_1 - T_2$ result depicted in Figure 3.5. One peak has $T_1 - T_2$ coordinates of 850 and 650 ms while the other has peaks centred on 150 and 110 ms. Control experiments show that the first peak is associated with sucrose while the second peak is associated with water. With two chemical species present in solution we may naively assume that the ratio of the integrated signals of the two peaks will be the ratio of the hydrogen content in the individual molecules, with allowance for the mass percent composition of the solution. Based on the mass percentage and the molecular formula of water and sucrose we predict an integrated signal ratio (sucrose/water) from the two peaks of 0.86. This is not the ratio observed experimentally which is 0.44.

We note that of the 22 hydrogens in the sucrose molecule 8 are on hydroxyl moieties and these hydrogens will exchange with the hydrogens of water. If we assume that such an exchange is rapid, which is the default assumption, then we would predict the ratio of non-exchangeable hydrogen in sucrose in proportion to the hydrogen in water plus the exchangeable hydrogen from sucrose, would be 0.42, which is much closer to the experimentally observed value.

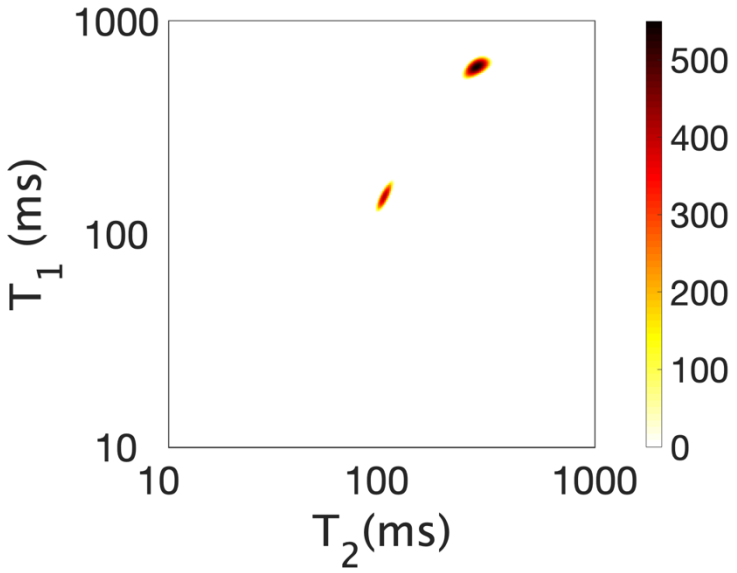

Figure 3.5 $T_1 - T_2$ measurement of a sucrose solution, 60% by mass. The integrated signal of the two peaks observed, as a ratio, was 0.44. The ratio of non-exchangeable to exchangeable hydrogens was calculated to be 0.42. The short T_2 corresponds to the non-exchangeable hydrogens on sucrose.

The $T_1 - T_2$ measurement will not record trace quantities of species dissolved in the liquid phase, but one can anticipate ready measurements of species that contribute several percent or more of the total H signal in solution.

3.4.6 D – T_2 Measurement

The *D* – T_2 measurement is a very powerful relaxation correlation measurement that characterizes species in the liquid state based on mobility through self-diffusion [28,29]. Species of interest may exist as discrete phases in the sample, for example water and oil, or they may coexist in solution.

The 60% sucrose solution above was also measured with a *D* – T_2 relaxation correlation measurement. This measurement is a simple modification of the bulk self-diffusion measurement described in section 3.4.3. Figure 3.6 shows the result of *D* – T_2 measurement of the sucrose solution, with two distinct peaks observed. The first peak has coordinates of 90 ms and 0.9 x 10^{-5} cm^2/s. The second peak has coordinates of 500 ms and 2 x 10^{-5} cm^2/s. Control experiments identify the second peak as being associated with water while the first peak with a reduced diffusion coefficient is associated with sucrose. The ratio of the integrated peak signals is 0.43, in agreement with the ratio anticipated for the case of exchangeable hydrogen on sucrose as outlined above.

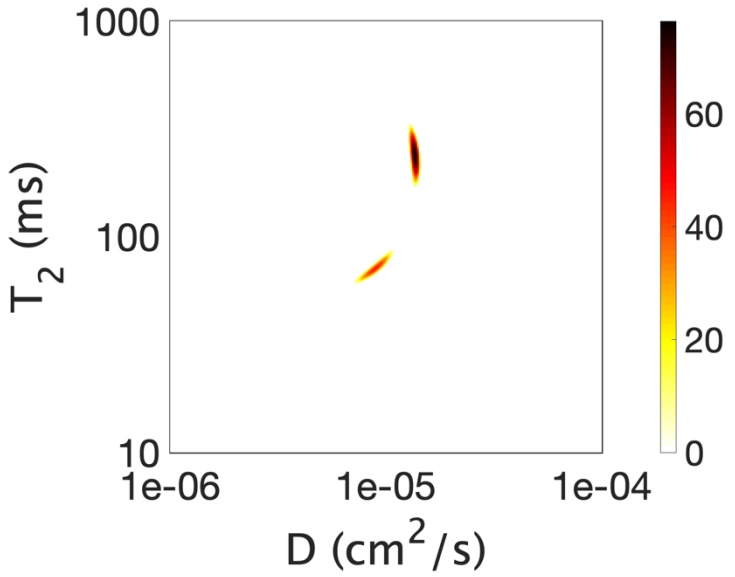

Figure 3.6 *D* – T_2 measurement of the sucrose solution. The integrated signal ratio of the two observed peaks was 0.43. The peak with reduced diffusion coefficient is associated with sucrose. The ratio of non-exchangeable to exchangeable hydrogens was calculated to be 0.42.

The experimentally determined *D* for water in the sucrose solution is not significantly reduced from the bulk value at 20˚C. This is no doubt in part due to limitations of the distribution measurement. The notable result here is not the absolute values of *D*, but rather discrimination of the two species in solution via *D* and T_2.

3.4.7 Depth Resolved Measurement

Portable MR is often employed in NMR well-logging, where T_1 – T_2 and *D* – T_2 correlations can distinguish between the fluid phases of hydrocarbon and water [28]. A distinct advantage to the Proteus magnet is its ability to be

submerged in solution permitting local composition analysis in a column of fluid. To demonstrate this capability, measurements were undertaken of a layered water and oil system. The oil layer was chosen to be cod liver oil while the water layer was copper sulfate doped distilled water. The ability to probe composition molecular behaviour as a function of depth in a liquid sample is not a new capability in MR, but one for which the Proteus magnet is ideally well suited. Figures 3.7a and 3.7b show $T_1 - T_2$ relaxation correlation measurements of the two layers in a beaker containing water and oil. The $T_1 - T_2$ results clearly characterizes the fluid species in each layer. The peaks observed in the $T_1 - T_2$ plots are consistent with relaxation lifetimes reported in this paper for the species employed. The experimental system of Figures 3.7a and 3.7b is intended as a model system for the very general problem of discriminating crude oil and water layers, often separated by an emulsion, in bulk storage tanks [30].

We should note the Proteus magnet's ability to measure changes in fluid properties while submerged depends on the ability of the fluid in the sample volume to be refreshed. The sensitive volume is more readily refreshed, either actively or passively, with a large diameter measurement volume.

(a)

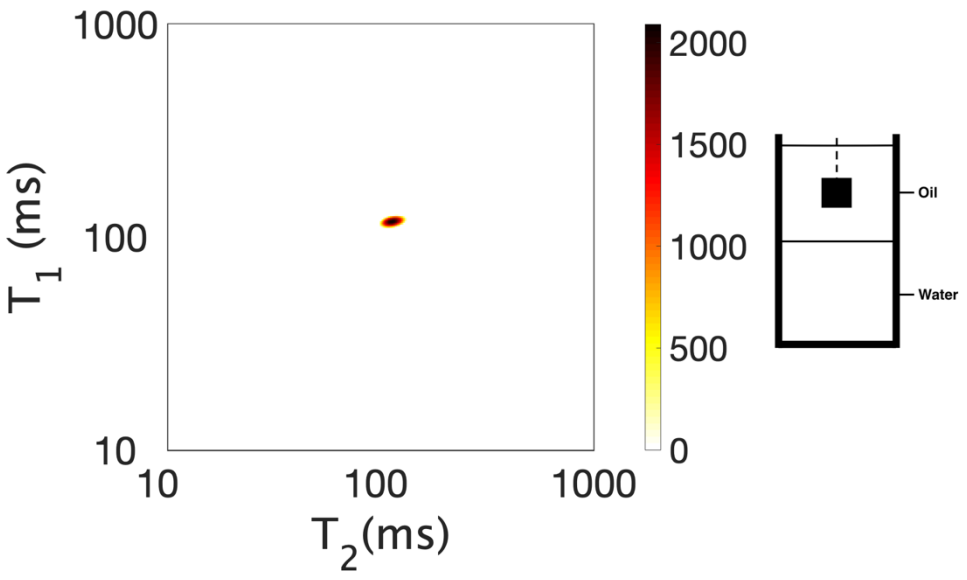

(b)

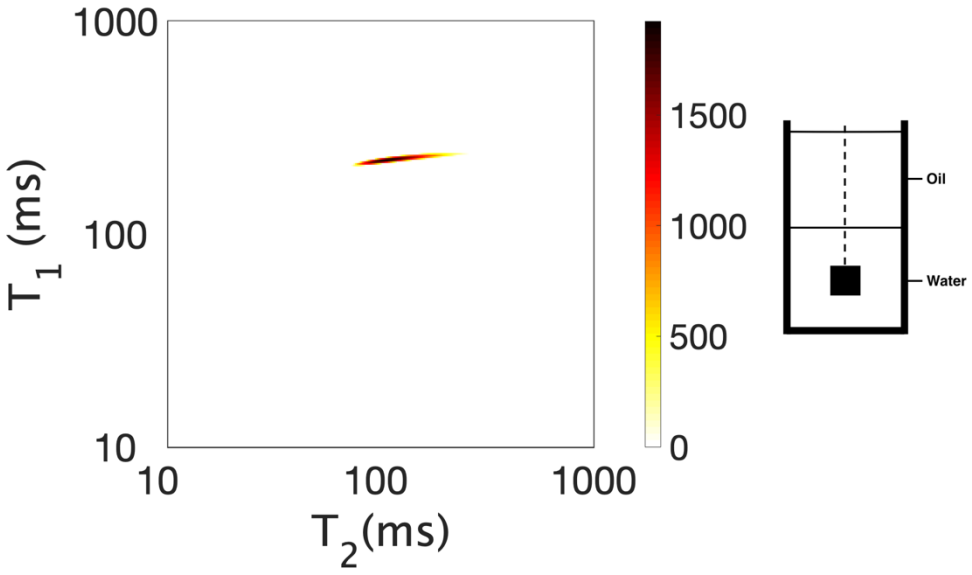

Figure 3.7 A depth resolved $T_1 - T_2$ measurement conducted by submersing the Proteus magnet into separate layers of oil and water. The two fluids are immiscible. (**a**) $T_1 - T_2$ measurement of the cod liver oil layer. The observed T_1 and T_2 agree well with the bulk T_1 and T_2 of cod liver. (**b**) $T_1 - T_2$ measurement of the $CuSO_4$ doped distilled water layer. The inset of each figure shows schematically the position of the sensor in the layered sample.

3.4.8 Depth Resolved Measurement

Alcohol content in antiseptic cleansers is a pressing legal and medical issue in many countries affected by Covid-19. Health Canada regulations currently requires distributors to include between 60–75% isopropanol in all sanitizers in order for them to be sold commercially [31]. $T_1 - T_2$ immersion measurements with the Proteus magnets are well suited to such determinations. Two commercial sanitizing solutions were chosen for analysis. A rubbing alcohol and a skin cleanser were chosen, composed of 99% and 70% isopropanol respectively. The anticipated ratio of non-exchanging hydrogens in rubbing alcohol (isopropanol) to exchangeable hydrogens in rubbing alcohol (water and isopropanol), was 0.15. The same ratio in the hand sanitizer was 0.55.

Figures 3.8a and 3.8b report $T_1 - T_2$ relaxation correlation measurements of the rubbing alcohol and the hand sanitizer respectively. The ratio of the integrated signal peaks observed from the rubbing alcohol was 0.13, whereas the ratio of the two peaks observed from the hand sanitizer was 0.49. Both experimental values closely agree with anticipated values. The shorter lifetime peak increases in amplitude as the concentration of isopropanol was decreased, the short lifetime peak is due to water and the exchangeable hydrogens in isopropanol. The amplification effect of exchangeable hydrogens permits a low water content isopropanol sample to be analyzed. Trace amounts could not be analyzed with this approach.

(a)

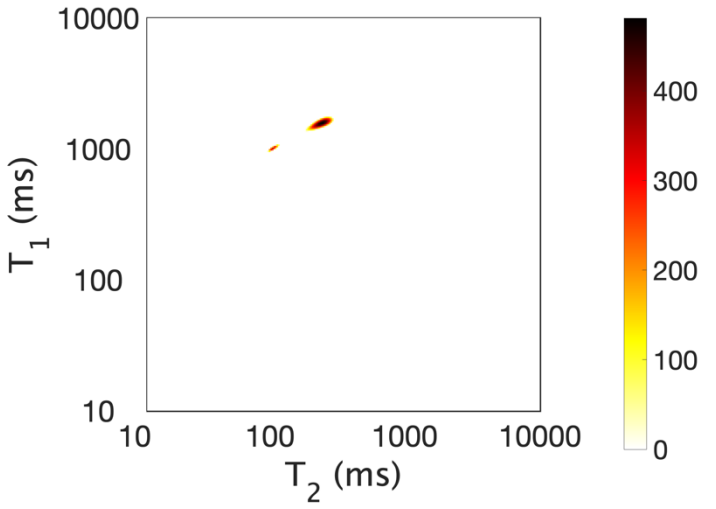

(b)

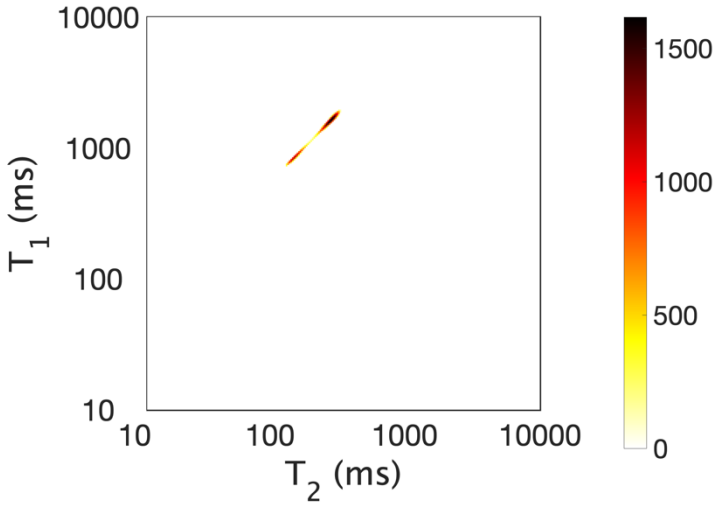

Figure 3.8 $T_1 - T_2$ measurement of isopropanol solutions. (**a**) $T_1 - T_2$ measurement of the 99% isopropanol rubbing alcohol where $\alpha = 1$. The integrated signal of the two peaks observed, as a ratio, was 0.13. The anticipated ratio was 0.15. (**b**) $T_1 - T_2$ measurement of the 70% isopropanol hand sanitizer where $\alpha = 0.1$. The integrated signal of the two peaks observed, as a ratio, was 0.49. The anticipated ratio was 0.55. In both figures the long T_2 lifetime peak corresponds to non-exchangeable hydrogens in isopropanol.

3.5 Conclusion

The Proteus magnet is a new and very simple style of enclosed portable magnet. These magnets are very flexible in terms of the relaxation-based measurements they may undertake. This means they will be very protean in their application.

A moderately homogenous static field in the sample space means these magnets are well suited to diffusion measurements including $D - T_2$. Analysis of solution properties and solution composition are possible through a variety of bulk relaxation time measurements including CPMG and $T_1 - T_2$.

The Proteus magnet is capable of undertaking a broad range of measurements in the field of engineering and material sciences. The most significant class of applications, reflective of the examples in the manuscript, will be measurements of solution composition. We note again that trace quantities will not be measurable. Phase change in a mixed fluid, for example precipitation and detection of the cloud point in oil solutions is an ideal application of the Proteus magnet. Small portable magnets are amenable to time-of-flight flow measurements and the Proteus magnet will be employed for such studies in the future [32].

The Proteus magnet in submerged operation is intended to equilibrate with the fluid to be measured. The temperature of the fluid will alter the magnetic

field produced, but this may be accommodated by retuning the RF probe. The RF probe is connected to an external tune-and-match circuit which is not immersed. The maximum operating temperature will be well below the magnet demagnetization temperature. The rated maximum operating temperature for NdFeB magnets depends on many factors, but 80˚C is a reasonable maximum operating temperature.

The Proteus magnet will function well at elevated fluid pressure since the box structure separating the magnets is filled with solid epoxy and the RF probe is immersed in the fluid to be measured. Mechanical deformation by isotropic compression (hydrostatic stress) will be limited by the bulk modulus of the materials employed, suggesting the possibility of enormous operating pressures. However, we can anticipate failure at much lower pressures due to heterogeneous materials in the Proteus magnet structure. High temperature and high pressure operation will be explored in future work.

The systematic design approach outlined in this paper permits one to explore the design of Proteus magnets that may be either smaller or larger than the design developed in this paper. Larger Proteus magnets, currently being explored, permit larger sample volumes and more uniform static fields in the sample space. Single shot bulk CPMG measurements of liquids is a logical and achievable experimental goal.

References

[1] Ross, M.M.B., Wilbur, G.W., Cano Barrita, P.F.J., Balcom, B.J. (2021), A Portable, Submersible, MR Sensor – The Proteus Magnet, J. Magn., Res 326, 106964.

[2] J. Mitchell, L.F. Gladden, T.C. Chandrasekera, E.J. Fordham, Low-field permanent magnets for industrial process and quality control, Prog. NMR Spect. 76 (2014) 1-60.

[3] B. Blümich, Introduction to compact NMR: A review of methods, Trends Analytical Chem. 83 (2016) 2-11.

[4] G. Eidmann, R. Savelsberg, P. Blümler, B. Blümich, The NMR MOUSE, a mobile universal surface explorer, J. Magn. Res. 122 (1996) 104-109.

[5] B. Blümich, P. Blümler, G. Eidmann, A. Guthausen, R. Haken, U. Schmitz, K. Saito, G. Zimmer, The NMR-mouse: construction, excitation, and applications, Magn. Res. Imag. 16 (1998) 479-484.

[6] A.E. Marble, I.V. Mastikhin, B.G. Colpitts, B.J. Balcom, An analytical methodology for magnetic field control in unilateral NMR, J. Magn. Res. 174 (2005) 78-87.

[7] S. Utsuzawa, E. Fukushima, Unilateral NMR with a barrel magnet, J. Magn. Res. 282 (2017) 104-113.

[8] E. Danieli, J. Perlo, B. Blümich, F. Casanova, Highly Stable and Finely Tuned Magnetic Fields Generated by Permanent Magnet Assemblies, Phys. Rev. Letters 110 (2013).

[9] Y.G. Linck, M.H.M Killner, E. Danieli, B. Blümich, Mobile Low-Field ^{1}H NMR Spectroscopy Desktop of Biodiesel Production, Appl. Magn. Reson. 44 (2013) 41-53.

[10] S. Meiboom, D. Gill, Modified spin-echo method for measuring nuclear relaxation times, Rev. Scientific Instruments 29 (1958) 688-69.

[11] F. Bloch, Nuclear induction, Phys. Rev. 70 (1946) 460.

[12] Y-Q. Song, L. Venkataramanan, M.D. Hürlimann, P. Frulla, C. Straley, T1–T2 correlation spectra obtained using a fast two-dimensional Laplace inversion, J. Magn. Res. 154 (2002) 261-268.

[13] H.Y. Carr, E.M. Purcell, Effects of diffusion on free precession in nuclear magnetic resonance experiments, Phys. Rev. 94.3 (1954).

[14] M.D. Hürlimann, L. Venkataramanan, Quantitative measurement of two-dimensional distribution functions of diffusion and relaxation in grossly inhomogeneous fields, J. Magn. Res. 157.1 (2002) 31-42.

[15] F. Díaz- Díaz, P.F. de J. Cano-Barrita, B.J. Balcom, S.E. Solís-Nájera, A.O. Rodríguez, Embedded NMR Sensor to Monitor Compressive Strength Development and Pore Size Distribution in Hydrating Concrete, Sensors 13 (2013) 15986-15999.

[16] T. Hughes-Riley, E.R. Dye, D.O. Anderez, F. Hill-Casey, M.I. Newton, R.H. Morris, Temperature dependence of magnetic resonance probes for use as embedded sensors in constructed wetlands, Sensors and Actuators A: Physical 241 (2016) 19-26.

[17] P.F. de J. Cano-Barrita, A.E. Marble, B.J. Balcom, J.C. García, I.V. Mastikhin, M.D.A. Thomas, T.W. Bremner, Embedded NMR sensor to monitor evaporable water loss caused by hydration and drying in Portland cement mortar, Cement and Concrete Research 39 (2009) 324-328.

[18] N. Sun, T.J. Yoon, H. Lee, W. Andress, R. Weissleder, D. Ham, Palm NMR and 1-chip NMR. IEEE Journal of Solid-State Circuits, 46(1) (2010) 342-352.

[19] D. J. Griffiths, Introduction to electrodynamics (4th ed.), Cambridge, United Kingdom: Cambridge University Press (2013) 229.

[20] G. Giovannetti, Comparison between circular and square loops for low-frequency magnetic resonance applications: theoretical performance estimation, Concept Magn. Res. 46 (2016) 146-155.

[21] M. Holz, S.R. Heil, A. Sacco, Temperature-dependent self-diffusion coefficients of water and six selected molecular liquids for calibration in accurate ^{1}H NMR PFG measurements, Physical Chemistry Chemical Physics 2.20 (2000) 4740-4742.

[22] E. Fukushima, S.B.W. Roeder, Experimental Pulse NMR: A Nuts and Bolts Approach, Westview Press, Boulder (1993) 378.

[23] M.D. Hürlimann, Ex situ measurement of one-and two-dimensional distribution functions, Single-Sided NMR, Springer, Berlin, (2011) 57-85.

[24] O. Petrov, J. Hay, I.V. Mastikhin, B.J. Balcom, Fat and moisture content determination with unilateral NMR, Food Research Int. 41 (2008) 758-764.

[25] A.E. Marble, I.V. Mastikhin, B.G. Colpitts, B.J. Balcom, A compact permanent magnet array with a remote homogeneous field, J. Magn. Res. 186 (2007) 100-104.

[26] S. Vashaee, M. Li, B. Newling, B. MacMillan, F. Marica, H.T. Kwak, J. Gao, A.M. Al-harbi, B.J. Balcom, Local T1-T2 distribution measurements in porous media, J. Magn. Res. 287 (2018)113-122.

[27] J. Mitchell, M.D. Hürlimann, E.J. Fordham, A rapid measurement of T1/T2: The DECPMG sequence, J. Magn. Res. 200 (2009) 198–206.

[28] S. Vashaee, B. Newling, B. MacMillan, F. Marica, M. Li, B.J. Balcom, Local diffusion and diffusion-T2 distribution measurements in porous media, J. Magn. Res. 278 (2017) 104-112.

[29] R.J.S. Brown, R. Chandler, J.A. Jackson, R.L. Kleinberg, M.N. Miller, Z. Paltiel, M. G. Prammer, History of NMR well logging, Concept Magn. Res. 13 (2001) 335–413.

[30] S.F.A. Bukhari, W. Yang, Multi-interface Level Sensors and New Development in Monitoring and Control of Oil Separators, Sensors 6 (2006) 380-389.

[31] Health Canada Health Products and Food Branch 2020: Guidance Document: Antiseptic Skin Cleansers (Domestic/Personal Use) Monograph. Available from: http://webprod.hc-sc.gc.ca/nhpid-bdipsn/atReq.do?atid=antiseptic_antiseptique&lang=eng.

[32] S. Richards, B. Newling, Measuring Flow Using a Permanent Magnet with a Large Constant Gradient, Appl. Magn. Reson. 50 (2019) 627-635.

Chapter 4: MR Measurement of Laminar Flow Employing a Proteus Magnet with Constant Magnetic Field Gradient

This chapter is largely based on a draft paper “MR Measurement of Laminar Flow Employing a Proteus Magnet with Constant Magnetic Field Gradient”, which may be submitted to the Journal of Magnetic Resonance. It describes the construction and application of a Proteus magnet with a constant magnetic field gradient intended for flow-oriented measurements.

The format of references in this chapter follows that of the destined journal.

4.1 Introduction

Magnetic resonance (MR) is advantageous for flow measurement since it is non-invasive and permits measurements of optically opaque samples [1]. The most important parameter to measure is the fluid velocity [2,3]. Multiple MR methods have been introduced to measure the flow velocity of liquids, including time-of-flight techniques, which rely upon the variation of signal magnitude with some variable encoding time to determine flow velocity *e.g.* [4]. However, phase shift methods are more common [5-7]. The constraint upon such flow measurements is that, in order to acquire phase shift, the employed instrument’s magnetic field must have either a constant gradient or pulsed gradient in the direction of flow [8].

Magnetic resonance imaging (MRI) flow studies are often performed in superconducting MR instruments, upon which are imposed the necessary flow sensitizing and spatial resolution gradients [9,10]. These systems are extremely powerful, permitting a range of measurements including imaging of complex flow. However, these are predominantly research instruments. In this paper we propose an alternative device to perform flow measurements based on a Proteus (PROTon Embedded sUbmersible Sensor) magnet modified to create a constant magnetic field gradient. Proteus magnets are portable, centre-field magnets, which generate a field through the employment of a pair of low-cost, nickel coated N52 grade NdFeB disk magnets, separated by a fixed-distance, with an RF coil placed between them [11]. In the present implementation, a magnetic field gradient, parallel to the gap between the magnets, is generated by pitching the two magnets away from the symmetry axis in a wedge-shaped geometry.

This new Proteus magnet has an increased sensitivity, compared to previous iterations, with disk magnets increased in size. Larger disk magnets permit stronger B_0 fields and a greater sample volume. Despite these changes, the flow-oriented Proteus magnet remains a simple portable sensor, which can be readily introduced into non-research environments. Design of the flow-oriented Proteus magnet emphasized simplicity of materials, while maintaining a size that permits the sensor to fit in one's hand. A simple phase shift measurement of tap water, undergoing laminar flow, permitted examination of

sensor performance. Multi-echo Carr-Purcell-Meiboom-Gill (CPMG) measurements are the basis of the measurement [12].

4.2 Theory

The CPMG pulse sequence, Eq. (4.1), consists of a $90_x°$ pulse followed by a series of $180_y°$ pulses, where each $180_y°$ pulse refocuses the magnetization to obtain an echo.

$$90^{\circ}_{\mathrm{x}} - \left(\tau - 180^{\circ}_{\mathrm{y}} - \tau - \mathrm{echo}\right)_n \qquad [4.1]$$

τ is the dephasing time, and n the number of echoes generated. Figures 4.1a and 4.1b illustrate this pulse sequence for the acquisition of single and multiple echoes respectively.

(a)

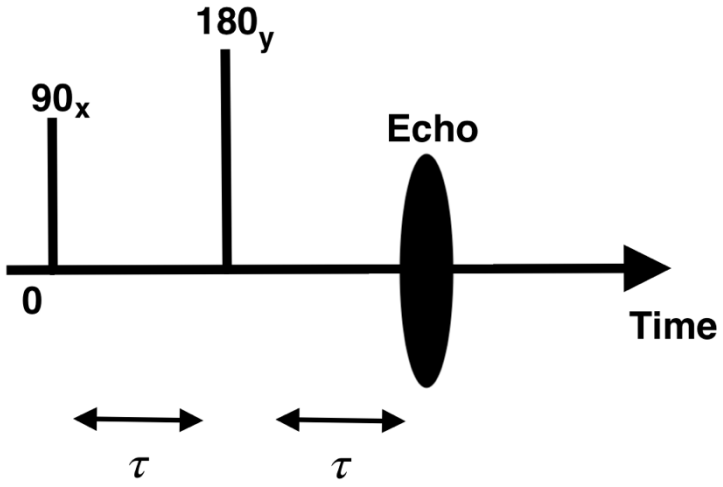

(b)

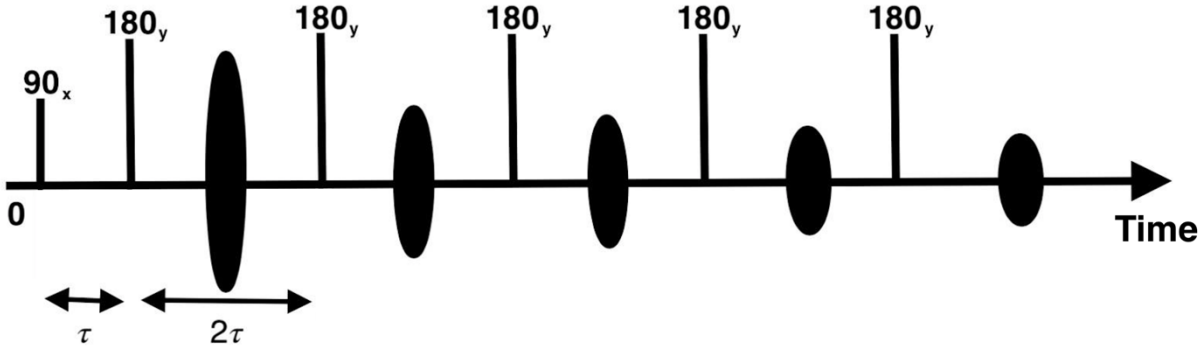

Figure 4.1 (a) The CPMG pulse sequence, where a $90_x°$ pulse followed by a $180_y°$ pulse refocuses the magnetization to obtain an individual echo. One implementation involves repeating measurements as a function of τ. (b) The CPMG pulse sequence where a $90_x°$ pulse followed by a series of n-$180_y°$ pulses refocuses the magnetization to obtain n-echoes. Another version of the measurements fixes the τ but employs multiple odd echoes.

A phase shift occurs for odd echoes in the CPMG measurement when fluid flows in the direction of a constant gradient G_x. For constant velocity, the phase accumulation ϕ can be expressed as Eq. (4.2), where γ is the gyromagnetic ratio and v is velocity [13].

$$\phi = \gamma v \int G_x(t)\, tdt = \gamma v G_x \int tdt \quad [4.2]$$

The velocity profile $v(r)$ through the cross-section of a circular pipe with laminar flow can be expressed as [14]

$$v(r) = \frac{wR^{\frac{1}{w}+1}}{w+1}\left(\frac{\Delta p}{2kL}\right)^{\frac{1}{w}}\left(1-\left(\frac{r}{R}\right)^{\frac{1}{w}+1}\right) \quad [4.3]$$

where Δp is the pressure drop along the circular pipe with a radius of *R* and a length of *L*, *k* is the fluid consistency coefficient, and *r* is the radial position. *w* is the flow behaviour index, which describes the fluid viscosity under strain. Based on Eq. (4.3), the volume flux *Q* can be expressed as

$$Q = \int_0^R 2\pi r v(r) dr = \frac{\pi w R^3}{1+3w}\left(\frac{\Delta p R}{2kL}\right)^{\frac{1}{w}} = v_{avg}\pi R^2 \quad [4.4]$$

The average velocity is thus $v_{avg} = \frac{\pi w R^3}{1+3w}$. For simplification, we define a variable $m = \frac{1}{w} + 1$. When a fluid such as water undergoes laminar flow, Reynolds number < 2000, through a circular pipe it is termed Poiseuille flow. The fluid viscosity is then independent of stress and has a known m = 2. The flow profile Eq. (4.3) can thus be expressed

$$v(r) = 2v_{avg}\left(1 - \left(\frac{r}{R}\right)^2\right) \qquad [4.5]$$

Where the maximum flow velocity v_{max} occurs at the centre of the pipe and is double the v_{avg}. Figure 4.2 illustrates, in cross section, Poiseuille flow of water in a pipe.

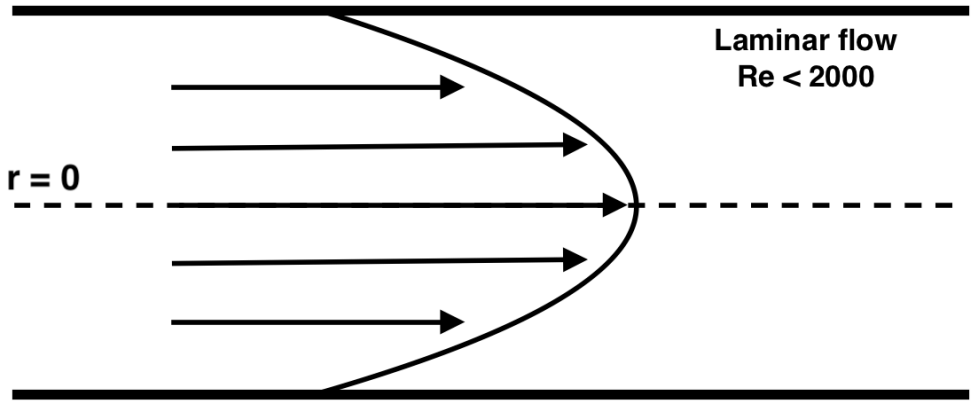

Figure 4.2 The Poiseuille flow profile of water in a pipe, where *m* = 2, as described in Eq. (5). The phase shift of each streamline depends on the gradient amplitude (assumed constant throughout the measurement volume) and the velocity indicated by vectors. Velocity at the wall will be 0. The average velocity of the flow will be half that of the maximum velocity along the centre line.

During CPMG measurement, the MR phase is reversed by each $180_y°$ pulse. For the first odd echo, phase accumulation can be calculated as Eq. (4.6), with the spatially resolved velocity substituted from Eq. (4.5) and an integration over *r* undertaken.

$$\phi_{odd} = -\gamma v G_x \int_0^{\tau} t dt + \gamma v G_x \int_{\tau}^{2\tau} t dt = \gamma v_{avg} G_x \tau^2 \quad [4.6]$$

This same approach also shows that phase accumulation cancels on all even echoes [15]. The relationship of Eq. (4.6) holds true for all odd echoes in a multiple-echo measurement. An experimental plot of ϕ versus τ^2 for a known G_x and γ yields a slope that is dependent on v_{avg}. This suggests it is possible to calculate the average flow velocity from the phase accumulation encoded in a series of odd echoes.

4.3 Experimental

4.3.1.1 Sensor Construction

Varying the distance between the two Proteus disk magnets, as a function of distance along the symmetry axis, will intuitively lead to a magnetic field gradient directed along the symmetry axis. This idea works remarkably well. The optimal separation and tilt angle for a desired constant gradient of 60 gauss/cm between the two N52 NdFeB K&J Magnetics (Pipersville, PA) disk magnets – 51 mm in diameter and 13 mm in thickness – was determined via

CST Studio Suite (Providence, RI). In simulation, each disk magnet was tilted at an angle of 1˚ from a starting separation of 14 mm between the magnets. 60 gauss/cm with this geometry was judged to be near ideal for the flow measurements envisaged. Figure 4.3 depicts two disk magnets, each rotated by 1˚ about the y axis.

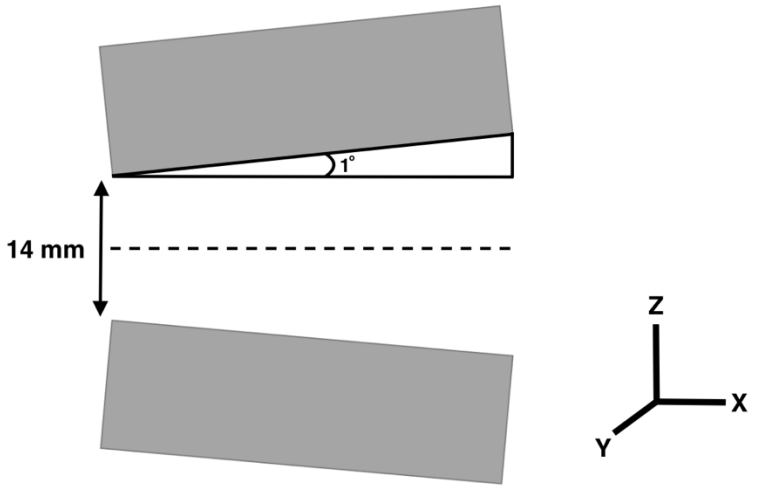

Figure 4.3 The tilted Proteus magnet. The sensitizing gradient G_x is along the symmetry axis, in the flow direction. Two N52 disk magnets - 51 mm in diameter and 13 mm in thickness - were separated by a 14 mm gap at one end and each pitched an angle of 1˚. This figure is not to scale.

A 60 x 60 x 40 mm casing fabricated from Garolite G-10 (McMaster Carr, Elmhurst, IL) was machined to house the magnets. The casing was divided into two separate pieces, where each piece had slots into which the magnets could be placed. Each slot was machined to permit the 1˚ tilt relative to the symmetry axis. The casing included a 10-mm diameter cylindrical hole at opposite ends of the shell, along the direction of the imposed gradient, to permit the placement of glass tubing to support the flow. A 4-turn solenoidal RF coil was loosely formed

around a glass pipe, 6.7 mm ID, and was capacitively matched to 50 Ω. The RF coil, fabricated from 0.8-mm-diameter copper wire, was centered in the Proteus magnet. The interior and exterior of the Proteus magnet was wrapped with 0.2 mm thick copper tape to limit external RF interference and suppress acoustic ringing.

Magnetic field plots of the sensitive spot in the Proteus magnet were acquired with a LakeShore 460 3-Channel Gaussmeter (Westerville, OH) connected to a BiSlide Positioning System and VXM Stepping Motor Controller (Velmex Inc., Bloomfield, NY). Magnetic field data was read and processed through a custom MATLAB script (Mathworks, Natick, MA).

4.3.1.2 Hardware

The RF probe was attached to a TecMag (Houston, TX) transcoupler with a λ/4 cable via BNC connectors. The transcoupler was joined to a Tomco Technologies (Stepney, Australia) 250-watt RF amplifier and a L3 Nard-MITEQ (Hauppauge, NY) 0.7 – 200 MHz preamplifier with a Mini-Circuits (Toronto, Ontario) 30 MHz low-band-pass filter.

4.3.2 Flow Network

The flow network was identical to the setup previously employed in [16] for time-of-flight flow experiments. In this configuration, a gravity-fed flow from a reservoir suspended several feet above the Proteus magnet was refreshed via a

pump from another reservoir at floor level to establish a constant flow through the Proteus magnet. To ensure a constant fluid level in the upper reservoir, and therefore a constant pressure head driving the flow, the pump provided more inflow to the upper reservoir than was flowing through the magnet. An overflow was installed in the upper reservoir to return excess water to the lower reservoir. A Masterflex Variable-Area Flowmeter (Cole-Parmer model # RK-32460-34, Montreal, Canada) was used to control and measure the average flow rate. The flowmeter provided a ground truth against which to compare the MR measurement. Flexible Fisherbrand clear PVC 0.8-cm-ID tubing (Fisher Scientific Company, Ottawa, Canada) was incorporated throughout the construction of the flow network except for the portion running through the magnet, where a 70-cm length of glass tubing with an ID of 0.67 cm was employed.

4.3.3 Measurements

Tap water containing 0.45wt% $CuSO_4$ was employed for average velocity flow measurements at 4.25, 6.60, and 9.00 cm/s, as set by the flowmeter. These velocities correspond to Reynolds numbers of 285, 440, and 600 respectively, below the threshold of turbulence. $CuSO_4$ is a contrast agent which reduces the water T_1 lifetime in a manner dependent on concentration [17]. For the copper sulphate solution, the measured T_1 = 50 ms. Realistic flow measurements would generally not employ a contrast agent. $CuSO_4$ was employed in these early

measurements to ensure that thermal equilibrium magnetization, $M_{0,}$ was achieved before entry into the RF probe for all streamlines [13]. The acquisition time of each measurement was ~ 2.5 min with a τ range, of 225-400 μs and a recovery time of TR = 250 ms. The $90_x°$ and $180_y°$ pulse durations were both 2.1 μs. CPMG echo trains, comprising 16 echoes, were acquired and manually phase corrected such that all even echo phases were zero. In the variable τ approach, error bars were determined by repetitive measurements. Three separate measurements were undertaken, and standard deviation determined. When multiple echoes were analysed, uncertainty was based on averaging the velocity determined from individual echoes. The uncertainty reported is the standard deviation.

4.4 Results

4.4.1 Field Plots

Figures 4.4a-c depict the simulated 2D magnetic field magnitudes of the tilted Proteus magnet in the Y-Z, X-Y, and X-Z planes respectively. Figure 4.4d is the 1D profile of the magnetic magnitude field along the central axis of the X-Z plane, taken from Figure 4.4c. The magnetic field has contributions from B_x, $B_{y,}$ and B_z, but in all cases B_z dominates. The disk magnets were axially separated by 14 mm, with each symmetrically rotated an angle of 1° to generate a design gradient of 60 gauss/cm. The proposed gradient strength was selected on the basis of ability to observe flow rates within an average velocity range of 1- 5

cm/s with echo times below 1 ms. The 60 gauss/cm gradient G_x is observed about the origin for a length of 15 mm, as illustrated in Figure 4.4d. Simulation shows, in the region of the RF probe, the gradient G_x varies to within 3 gauss/cm when symmetrically displaced 3.45 mm off the central axis in the X-Y plane and within 2 gauss/cm in the X-Z plane.

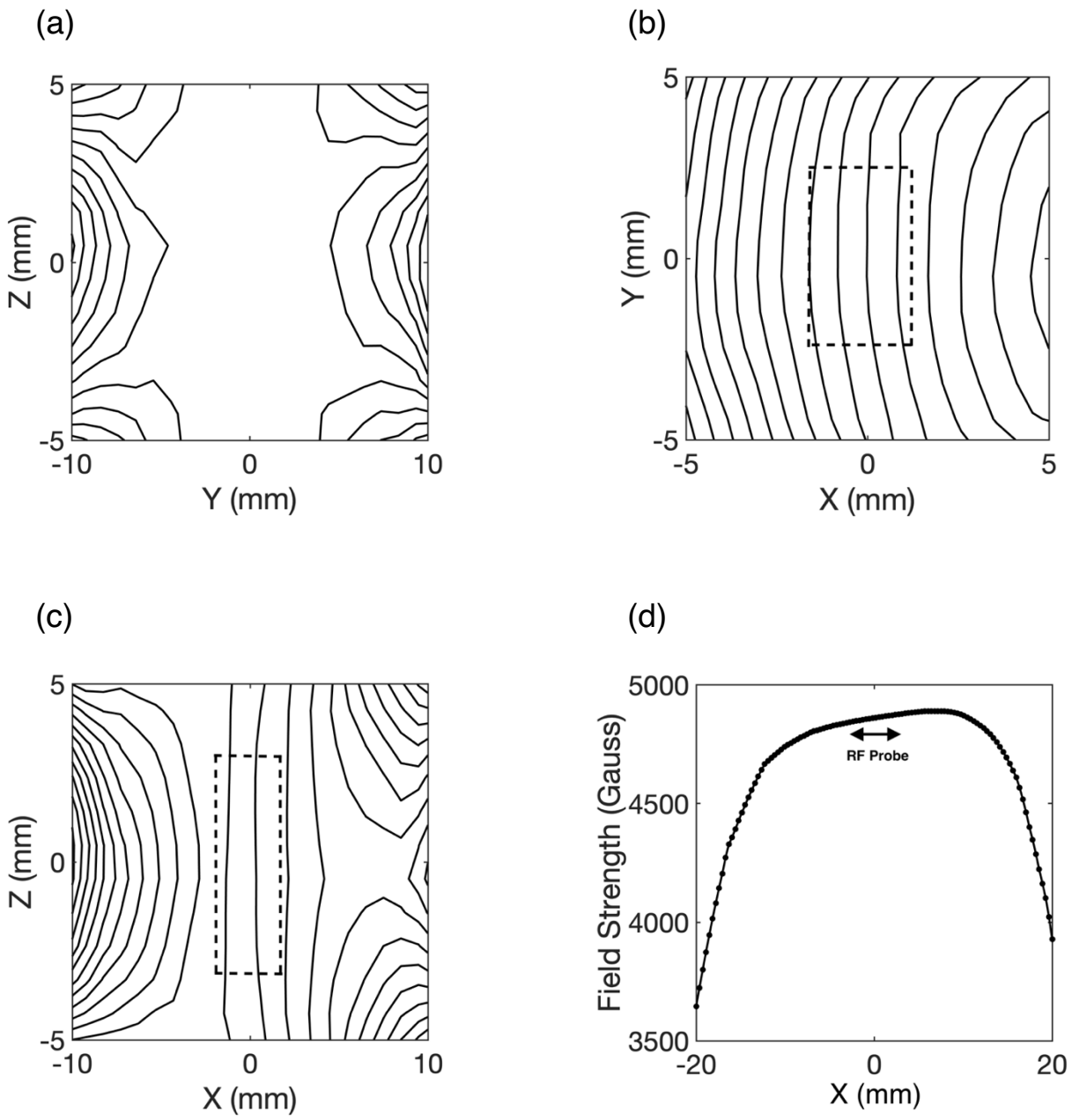

Figure 4.4 The simulated 2D and 1D magnetic field magnitudes of the tilted Proteus magnet in the central 2D Y-Z, X-Y, and X-Z axis planes. An RF coil with a length of 3.2 mm and ID of 6.7 mm is placed in the desired measurement volume and highlighted in b-d. (a) The field plot in the Y-Z plane is largely uniform within the volume of interest. The field contour interval is 7 gauss. (b)&(c) Illustrate the constant gradient within the central region of the magnet that extends ~ 15 mm in X, ~ 7 mm in Y and ~ 10 mm along Z. Field contour intervals are 6 and 12 gauss respectively. (d) The 1D field plot along the central line of the ZX transverse plane, obtained from (c). The constant gradient can be observed ~ 15 mm about the center of the Proteus magnet.

In order to ensure that the phase shift measured would be observed in a region of constant gradient, an RF coil with a length of 3.2 mm and ID of 6.7 mm - sample volume 110 mm^3 – was employed and placed in the centre most region.

Figure 4.5 is the experimental field plot of 1D magnetic field magnitude along the X central axis, Y = 0, Z = 0. As before, the magnetic field has contributions from B_x, B_y, and B_z. The finite size of the field sensor permitted only on axis measurement. From simulation, the region of constant gradient, on axis, was $\pm$ 15 mm about the origin. The experimental field plot showed the region of constant gradient was reduced to 6 mm compared to simulation. The experimental field plot yields a G_x value, near the origin, of 64 gauss/cm. The discrepancies in spatial extent and G_x value from simulation are likely due to non-ideal disk magnets as well as imperfections in the built shell, which houses the magnets. The RF probe was centered about the magnet origin. The Proteus magnet was tuned to a frequency of 20.48 MHz for ^1H. Average velocity measurements of known water flow were performed to confirm the G_x gradient amplitude.

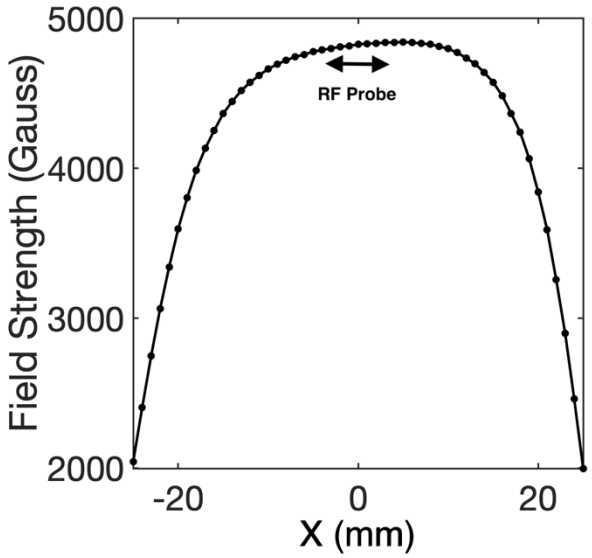

Figure 4.5 The experimental 1D field magnitude measured along X with Y = 0, Z = 0 of the 1˚ tilted Proteus magnet. The field strength and region of the desired constant gradient are determined coarsely compared to the simulated results, but are, nevertheless, similar. The RF coil of length 3.2 mm and ID of 6.7 mm - sample volume 110 mm^3 - was placed about the central region of the Proteus magnet. Discrepancies observed in the experimental field results compared to the simulated field are likely indicative of imperfections in the disk magnets or in the geometry of the custom shell housing.

4.4.2 Constant Gradient

To demonstrate the utility of the modified Proteus magnet we undertook measurements of the average velocity of doped tap water. We note here that we do not need to take into account the effects of intrinsic spin-spin relaxation or self-diffusion in the phase shift acquisition, as these attenuations do not alter phase. However, while neither influence the phase shift, each affects the intensity of the signal and therefore the real and imaginary signal amplitudes. Thus, as dephasing time τ is increased or as additional echoes are acquired, the

overall signal is reduced. Uncertainty in the real and imaginary signal components propagates to increased phase angle uncertainty.

The T_1 of the tap water solution was measured to be 50 ms. The $CuSO_4$ doping was employed in order to ensure full polarization of water ^1H as it enters the detector, based on an estimated polarization time of 1.5 cm/v_{avg}. The polarization length was judged from the simulated field plot to be 1.5 cm. For Poiseuille flow with an average velocity of 4.25 cm/s, the maximum velocity will be 9.50 cm/s. For these velocities, with an estimated entry length of 1.5 cm, the polarization times will be 350 ms and 150 ms. Given the T_1 of 50 ms, the M_Z polarization is estimated to be 100% and 95% of M_0 respectively.

A phase measurement employing the relationship of Eq. (4.6) was performed in order to calibrate the gradient. Fixing the flow meter to an average velocity of 4.25 cm/s, CPMG measurements at a range of τ times were performed to determine phase versus τ^2. These CPMG measurements follow those described in Figure 4.1a, as only the phase shift encoded in the first echo was employed. Figure 4.6 illustrates the real and imaginary signal components of a CPMG echo train with τ = 225 μs at an average velocity of 4.25 cm/s. Alteration of the signal components is observed for the odd echoes.

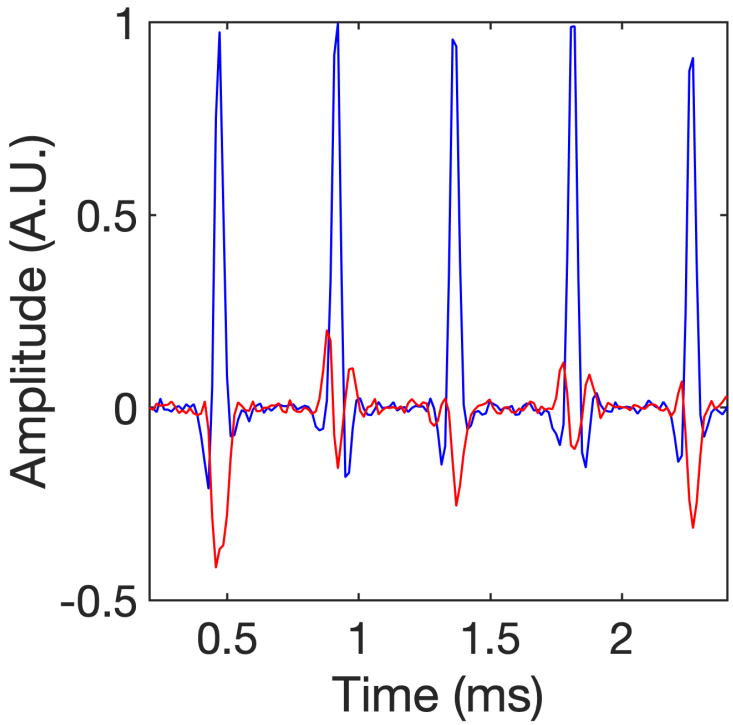

Figure 4.6 The CPMG echo train measurement of $CuSO_4$-doped tap water undergoing laminar flow at an average velocity 4.25 cm/s and τ = 225 μs. The real and imaginary signals are represented by blue and red respectively. The odd echoes undergo a phase shift compared to even echoes. The odd echo phase shift permits calculation of the mean velocity through Eq. (4.6).

For a CPMG measurement of doped tap water flowing at 4.25 cm/s, with τ = 225 µs, the real and imaginary signal components at the peak of the first odd echo are Re = 7.56 $\pm$ 0.81 and Im = -2.97 $\pm$ 0.35 in arbitrary units. Based on propagation of uncertainties the phase angle uncertainty is $\pm$ 0.04 radians, with a phase angle of 0.37 radians. This phase angle uncertainty is similar to the uncertainty determined from multiple measurements.

Figure 4.7 depicts the velocity encoded phase shift of the first odd echo acquired across a range of τ^2 values. The linearity of the plot confirms the

fundamental measurement, fitting the slope to Eq. (4.6) with the intercept set to (0,0), with a known velocity, yielded a gradient of 65 ± 0.8 gauss/cm. This value is close to the simulated result but agrees well with the gradient measured using the Lakeshore Gaussmeter which has a known uncertainty of 0.125%. The experimentally determined G_x gradient, 65 gauss/cm, was employed in all subsequent work. The design gradient value is less reliable than this experimentally determined gradient due to construction limitations discussed above.

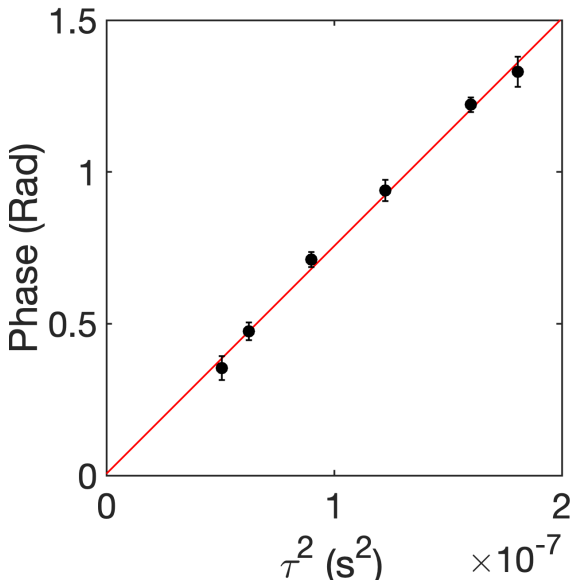

Figure 4.7 Plot of phase shift of the first odd echo against τ^2 to determine G_x. The known average velocity was 4.25 cm/s. This method employs the pulse sequence shown in Figure 1a. The phase change was fitted through (0,0) to the linear expression of Eq. (4.6). The constant gradient was determined to be 65 ± 0.75 gauss/cm. This value is in close agreement with the experimental field plot gradient of 64 gauss/cm.

Eq. (4.6) suggests that with a known G_x and fixed τ, it is possible to measure velocity with a single echo phase shift. Indeed, Eq. (4.6) and previous

discussion suggest we can measure single phase shifts from multiple odd echoes and therefore multiplex the measurement. We now explore this capability with 3 different average velocities of doped water, 4.25, 6.60, and 9.00 cm/s with τ set to 225 μs. A single CPMG decay measurement with multiple echoes is undertaken, as in Figure 4.1b, with a 4τ time interval between each odd echo peak. The echo amplitude decays along the echo train. For that reason, the phase shift from only the first five odd echoes was acquired. Figure 4.8 shows individual velocity measurements (phase) from the first five odd echoes for each bulk velocity. The mean velocities, based on the calculated phase of the first 5 odd echoes, were determined to be 4.14 ± 0.10, 6.88 ± 0.29, 9.19 ± 0.48 cm/s. The later echo results are clearly less reliable than early odd echo measurements. Low velocity flow was also seemingly easier to measure. Results are in close agreement with the expected average velocity, and we note that the uncertainties increase at higher flow rates as signal-to-noise ratio decreases. The consistency between results indicates that the modified Proteus magnet can readily determine basic flow properties and may be applied to more complex studies in the field of rheology.

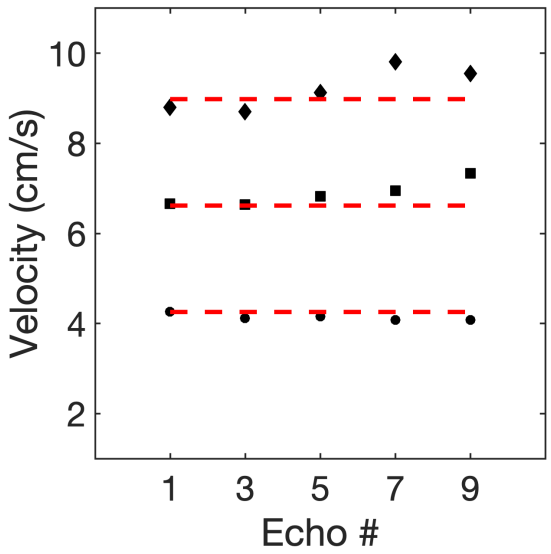

Figure 4.8 Plot of the average velocity determined from each of the first five odd echoes in a CPMG measurement for known average velocities of 4.25 (●), 6.60 (■) and 9.00 (♦) cm/s. Based on Eq. (4.6), each odd echo in the CPMG measurement should measure the same phase and, hence, the same velocity. This measurement employs the pulse sequence of Fig 1b. The dashed red lines indicate the known average velocities. Measured average flow rates were found to be 4.14 ± 0.10, 6.88 ± 0.29, and 9.19 ± 0.48 cm/s for the three known flows.

4.5 Conclusion

We have demonstrated that the Proteus magnet geometry can be manipulated to generate a constant magnetic field gradient in order to perform simple flow experiments. A 1˚ pitch is difficult to achieve experimental validation in the present flow régime, but different angles can be employed to generate larger gradients based on the desired outcome. As disk magnets are inexpensive, it is practical to construct countless variations on the Proteus magnet design, making it a multifaceted instrument for both research and practical usage. We found that phase shift and, hence, average velocity can be

reliably measured with a palm sized Proteus magnet. The Proteus magnet may be of utility in characterizing more complex flows [18,19].

References

[1] Gladden, L. F., & Sederman, A. J. (2013). Recent Advances in Flow MRI. Journal of Magnetic Resonance, 229, 2-11

[2] Singer, J. R. (1959). Blood Flow Rates by Nuclear Magnetic Resonance Measurements. Science, 130(3389), 1652-1653.

[3] Ahmadi, S., & Mastikhin, I. (2020). Velocity Measurement of Fast Flows Inside Small Structures with Tagged MRI. Applied Magnetic Resonance, 1-18.

[4] Osán, T. M., Ollé, J. M., Carpinella, M., Cerioni, L. M. C., Pusiol, D. J., Appel, M., & Espejo, I. (2011). Fast measurements of average flow velocity by Low-Field 1H NMR. Journal of Magnetic Resonance, 209(2), 116-122.

[5] Caprihan, A., & Fukushima, E. (1990). Flow Measurements by NMR. Physics Reports, 198(4), 195-235.

[6] Singer, J. R. (1978). NMR Diffusion and Flow Measurements and an Introduction to Spin Phase graphing. Journal of Physics E: Scientific Instruments, 11(4), 281.

[7] Stepišnik, J. (1985). Measuring and Imaging of Flow by NMR. Progress in Nuclear Magnetic Resonance Spectroscopy, 17, 187-209.

[8] Gibbs, S. J., & Johnson Jr, C. S. (1991). A PFG NMR experiment for Accurate Diffusion and Flow Studies in the Presence of Eddy Currents. Journal of Magnetic Resonance, 93(2), 395-402.

[9] Adair, A., Balcom, B. J., & Newling, B. (2020). Velocity Mapping of Fast Flows using a Linearly Ramped Gradient Waveform. Journal of Magnetic Resonance, 106754.

[10] Gauthier, A. R. P., & Newling, B. (2018). Gas Flow Mapping in a Recorder: An Application of SPRITE MRI. Applied Magnetic Resonance, 49(10), 1151-1162.

[11] Díaz-Díaz, F., Cano-Barrita, D. J., Prisciliano, F., Balcom, B. J., Solís-Nájera, S. E., & Rodríguez, A. O. (2013). Embedded NMR sensor to Monitor Compressive Strength Development and Pore Size Distribution in Hydrating Concrete. Sensors, 13(12), 15985-15999.

[12] Meiboom, S., & Gill, D. (1958). Modified Spin-echo Method for Measuring Nuclear Relaxation Times. Review of Scientific Instruments, 29(8), 688-691.

[13] D.G. Nishimura, Principles of Magnetic Resonance Imaging, 23–98 & 203–212. lulu.com (2010)

[14] Hinch, E. J. (2004). Lecture 3: Simple Flows. Woods Hole Oceanographic Institution. Retrieved March 05, 2021, from https://gfd.whoi.edu/gfd-publications/gfd-proceedings-volumes/2003-2/

[15] Pope, J. M., & Yao, S. (1993). Quantitative NMR Imaging of Flow. Concepts in Magnetic Resonance, 5(4), 281-302.

[16] Richard, S. J., & Newling, B. (2019). Measuring Flow Using a Permanent Magnet with a Large Constant Gradient. Applied Magnetic Resonance, 50(5), 627-635.

[17] Pierre, V. C., & Allen, M. J. (Eds.). (2017). Contrast agents for MRI: Experimental Methods. Royal Society of Chemistry.

[18] Blythe, T. W., Sederman, A. J., Stitt, E. H., York, A. P., & Gladden, L. F. (2017). PFG NMR and Bayesian Analysis to Characterise Non-Newtonian fluids. Journal of Magnetic Resonance, 274, 103-114.

[19] Cheung, M. K., Powell, R. L., & McCarthy, M. J. (1997). Nuclear Magnetic Resonance Imaging Based Capillary Rheometer. AIChE journal, 43(10), 2596-2600.

Chapter 5: Conclusions and Future Work

Techniques for designing and testing a portable MR sensor - dubbed the Proteus magnet - for fluid composition and velocity related phase shift have been demonstrated. By optimizing the sample volume and field strength the SNR of CPMG based measurements was maximized, permitting fast measurements. Analytical methodologies were employed to obtain the optimal geometry to generate suitable magnetic fields utilizing NdFeB disk magnets. The first discussed Proteus magnet, with a reasonably homogeneous field, was coated in cured epoxy and submersed in fluids to perform ordinary relaxation measurements. The second Proteus magnet generated a field with a constant magnetic field gradient which was oriented along the direction of fluid flow in a glass pipe.

The epoxy-coated Proteus magnet was assessed with a series of CPMG based measurements including, T_1, T_2, $T_1 - T_2$, and $D - T_2$. $T_1 - T_2$, and $D - T_2$ measurements were performed to characterize the composition of mixed solution. It was found that the Proteus magnet could readily distinguish the quantity of species within the solution, with concentrations as low as 1% in one case. The constant magnetic field gradient Proteus magnet was tested by acquiring the phase shift of doped tap water flowing in a glass pipe parallel to the direction of the gradient. The relationship between the phase shift and

constant gradient amplitude permitted a reliable calculation of the fluid flow mean-velocity.

Due to the multifaceted nature of the Proteus magnet, there are multiple avenues in which future work could be directed. Further exploration of the submersible Proteus magnet would focus around applying it to fluid composition relaxation tasks that benefit from the application of a small, inexpensive, MR sensor. One such option is the exploration of T_2^* decay as measured through FIDs, which was found to be possible. The magnetic fields tendency to equilibrate with the fluid measured is another possible benefit that warrants application. Temperature will affect the amplitude and distribution of the magnetic field; however, the RF probe is amendable to retuning at variable temperatures. The ability to adjust the frequency of the RF probe in a Proteus magnet would furthermore permit the analysis of other nuclei such as ^{7}Li, or ^{19}F. Lastly, larger disk magnet combinations can be applied to generate stronger fields and sample volumes – increasing the overall sensitivity of CPMG measurements.

The constant gradient Proteus magnet has significant application to MR related rheology studies. The angle of rotation between the two disk magnets is only 1°, however larger angles can be employed to generate stronger gradient amplitudes, thus the autonomy of the design permits customization for different measurements. The current procedure in this thesis demonstrates the

methodology by which the mean velocity of a fluid flow can be obtained via flow phase shift. However, the ability to determine the maximum velocity and therefore the fluid type based on the flow profile has been neglected. Developing a technique to characterize the flow profile of the liquid and classify the fluid as either shear-thinning, shear-thickening, or Newtonian directly from CPMG based measurements would be of great interest.

Curriculum Vitae

Candidate's full name: Michael Murray Brooker Ross

Journal Publications:

[1] Ross, M.M.B., Wilbur, G.W., Cano Barrita, P.F.J., Balcom, B.J. (2021), A Portable, Submersible, MR Sensor – The Proteus Magnet, J. Magn., Res 326, 106964.

[2] Guo, J., Ross, M.M.B., Newling, B., & Balcom, B.J. (2021), Non-Newtonian Fluid Velocity Profiles Determined with Simple Magnetic Resonance Echoes, Phys. Rev. Applied (submitted)

U.S. Patent Applications:

[1] Ross, M.M.B., Balcom, B.J. (2021), MAGNETIC RESONANCE PROBE AND METHOD

[2] Guo, J., Ross, M.M.B., Newling, B., Balcom, B.J. (2021), MAGNETIC RESONANCE METHODS AND DEVICES FOR CHARACTERIZING RHEOLOGICAL PROPERTIES OF A FLUID (Provisional)